OUKA
The University of Osaka
Institutional Knowledge Archive

Title	Research on the thermal conductivity of MOX fuel with heterogeneous plutonium distribution
Author(s)	北野, 剛司
Citation	大阪大学, 2026, 博士論文
Version Type	VoR
URL	https://doi.org/10.18910/105462
rights	
Note	

The University of Osaka Institutional Knowledge Archive : OUKA

https://ir.library.osaka-u.ac.jp/

The University of Osaka

Doctoral Dissertation

Research on the thermal conductivity of MOX fuel with heterogeneous plutonium distribution

KITANO Koji

January 2026

Graduate School of Engineering,
The University of Osaka

Abstract

Mixed oxide (MOX) fuel, composed of plutonium (Pu) and uranium (U) is used in light water reactors for effective use of uranium resources. The current commercial MOX fuel is fabricated via the micronized master blend (MIMAS) process for mixing plutonium oxide and uranium oxide powders. The MOX fuel fabricated via the MIMAS process exhibits a heterogeneous microstructure characterized by agglomerates with higher Pu concentrations compared to the surrounding fuel matrix. Thermal conductivity is an important fuel property because most fuel properties and behaviors are temperature dependent. Accordingly, the thermal conductivity of MIMAS–MOX fuel has been the subject of numerous studies. Nevertheless, the effect of heterogeneous Pu distribution on thermal conductivity remains insufficiently understood and inadequately modeled. The objectives of this study are to explain the mechanism how the heterogeneous Pu distribution gives an effect on overall thermal conductivity and to formulate its effect. Initially, we conducted experimental investigations on the thermal conductivity of unirradiated UO_2, which became the foundational basis for understanding and formulating the thermal conductivity of MIMAS-MOX fuel. Subsequently, we focused on thermal resistivity rather than thermal conductivity and derived factors to correct the thermal resistivity of unirradiated UO_2 to that of unirradiated and irradiated (U, Pu)O_2. To model the effect of heterogeneous Pu distribution, we applied the analogous process for combining electric resistances to thermal resistances. Pu concentration maps obtained via EPMA were converted to thermal resistance maps using the thermal resistivity of unirradiated UO_2 and the correction factors to (U, Pu)O_2. The effective thermal conductivity, representing the overall thermal conductivity of the MIMAS-MOX fuel, was derived by assuming series connection and parallel configurations of the local thermal resistances in the map. These processes were formulated into the equation. The effective thermal conductivity, derived from the formula, agreed with the thermal conductivity measurements well. The results demonstrate that U-rich phase containing less Pu serves as fast pathways for thermal conduction in MIMAS-MOX fuel.

Contents

1. Introduction 8

2. Thermal conductivity measurements for single crystalline and polycrystalline UO_2 10

2-1 Material 10

2-2 Method 10

2-2-1 Sample observation 10

2-2-2 Method of thermal conductivity measurement 11

2-3 Results 12

2-3-1 Results of sample observation 12

2-3-2 Results of thermal conductivity measurement 13

2-4 Discussion 15

2-4-1 Application of the results to thermal conductivity of MOX fuel 15

3. Thermal conductivity measurement for unirradiated and irradiated MOX fuels 18

3-1 Material 18

3-1-1 Sampled fuels 18

3-1-2 Samples for thermal conductivity measurement 20

3-2 Method 21

3-2-1 Sample observation 21

3-2-2 Method of thermal conductivity measurement 23

3-3 Results 25

3-3-1 Results of sample observation 25

3-3-2 Results of thermal conductivity measurement 36

3-4 Discussion 39

3-4-1 Discussion on the relation between Pu distribution and burnup distribution 39

3-4-2 Discussion on the effect of oxygen to metal ratio on thermal conductivity 40

3-4-3 Discussion on the effect of plutonium on thermal conductivity 41

4. Modeling of the thermal conductivity of MOX fuel with heterogeneous Pu distribution ... 43

4-1 Modeling of thermal resistivity of U-Pu mixed oxide 43
4-1-1 Relation of phonon scattering and thermal resistivity 43
4-1-2 Effect of Pu content on thermal resistivity 45
4-1-3 Effect of burnup on thermal resistivity 49
4-1-4 Correction for Pu content 51
4-1-5 Thermal resistivity of homogeneous MOX fuel 51
4-2 Modeling of thermal resistivity and conductivity of heterogeneous MOX fuel 53
4-2-1 Model to combine thermal resistivities connected in series and parallel 53
4-2-2 Application to the heterogeneous MOX fuel 57
4-3 Evaluation of the thermal conductivity of heterogeneous MOX fuels 58
4-3-1 Analysis of thermal resistivity and conductivity using Pu mapping 58
4-3-2 Comparison of model predictions and measurements 65
5. Conclusion 71

List of tables

Table 1 Characteristics of fabricated samples 13
Table 2 Specifications of the fuel rods irradiated in the Halden reactor [31] 19
Table 3 Specifications of the fuel rods irradiated in the BR3 and BR2 reactor [32]..... 19
Table 4 Fuel rod burnups after the irradiation test at the Halden reactor [31] 20
Table 5 Fuel rod burnup after the irradiation test at the BR2 reactor [16] 20
Table 6 Samples subjected to thermal conductivity measurement [16] 21
Table 7 Statistical data of the measurements via EPMA and EBSD on the MIMAS-MOX fuel with 8.4 % Pu [30] 30
Table 8 Statistical data of the measurements via EPMA and EBSD on the MIMAS-MOX fuel with 14.3 % Pu [30] 31
Table 9 The ratios of plutonium and neodymium contents among U agglomerate, intermediate phase and Pu-rich agglomerate. 40
Table 10 Functions to model the effects of burnup on thermal resistivity and modeling functions [58] 50
Table 11 Average Pu contents and thermal resistivity of the three phases at 1000 K in the unirradiated MIMAS–MOX fuel shown in Table 7 60
Table 12 Burnup, residual initial Pu content, and thermal resistivity of the three phases in MIMAS–MOX fuel shown in Table 11, assuming irradiation up to 68 GWd/t-HM and a temperature of 1000 K 61
Table 13 Volume fractions of the sections measured via image analysis on Figure 25 . 62
Table 14 Result of the evaluation on average thermal resistivity of the sections shown in Figure 25 and effective thermal conductivity in the unirradiated state at a temperature of 1000 K 62
Table 15 Result of the evaluation on thermal resistivity and conductivity of the sections shown in Figure 25 and effective thermal conductivity assuming a burnup of 68 GWd/t-HM 63

Table 16　Effective thermal conductivities evaluated from four ternary Pu concentration maps for the two kinds of MIMAS–MOX fuels and the evaluated thermal conductivity of SBR–MOX fuel at a temperature of 1000 K 64

List of figures

Figure 1 XRD patterns of single crystalline (sc) and polycrystalline (pc) UO_2 12

Figure 2 EBSD image of polycrystalline UO_2 (2000x) 13

Figure 3 Thermal conductivity of single crystalline and polycrystalline UO_2 with a theoretical density of 100 % [15] 14

Figure 4 Thermal resistivity of unirradiated single-crystalline and polycrystalline UO_2 with a theoretical density of 95 % 15

Figure 5 Grain size dependence of thermal conductivity at 300 K, 500 K, and 1000 K for UO_2 17

Figure 6 Thermal conductivities converted from thermal diffusivities measured under thermal cycles [1] 25

Figure 7 Overlapped image from the EPMA and EBSD on the MIMAS-MOX fuel 8.4 % Pu [30] 26

Figure 8 Overlapped image from the EPMA and EBSD on the MIMAS-MOX fuel with 14.3 % Pu [30] 27

Figure 9 Ternary phase map consisting of the U agglomerate, intermediate phase, and Pu-rich agglomerate on the MIMAS-MOX fuel with 8.4 % Pu [30] 28

Figure 10 Ternary phase map consisting of the U agglomerate, intermediate phase, and Pu-rich agglomerate on the MIMAS-MOX fuel with 14.3 % Pu [30] 28

Figure 11 Ceramography on the cross-section of fuel rods after irradiation [1] 32

Figure 12 Pu mapping at different radial positions on the SBR-MOX fuel irradiated up to 64.2 GWd/t in the Halden reactor [1] 33

Figure 13 Pu mapping at different radial positions on the MIMAS-MOX fuel irradiated up to 63.7 GWd/t in the Halden reactor [1] 33

Figure 14 Pu mapping on the MIMAS-MOX fuel samples taken from different axial positions of the two fuel rods irradiated in the R2 reactor [1] 34

Figure 15 Nd content measured with EPMA line scanning along the radius on the

MIMAS-MOX fuel irradiated up to 63.7 GWd/t in the Halden reactor [29] ... 35
Figure 16 Elemental analysis across a Pu rich agglomerate on the sample irradiated at a high LHR up to a burnup of 35 GWd/tHM [39] ... 36
Figure 17 Thermal conductivity of unirradiated and irradiated UO_2, SBR-MOX, and MIMAS-MOX fuels with 95 % TD [16] ... 37
Figure 18 Thermal conductivity of UO2, SBR-MOX, and MIMAS-MOX fuels irradiated in the Halden reactor [16] ... 38
Figure 19 Thermal conductivity of MIMAS-MOX fuels irradiated in the Halden reactor and the BR2 reactor [16] ... 39
Figure 20 Thermal resistivity of MOX fuels as a function of Pu content ... 46
Figure 21 Ratio of the thermal resistivity of MOX fuel to that of UO2 fuel as a function of Pu content ... 49
Figure 22 Comparison of prediction with measurements on thermal conductivity of MOX fuel with homogeneous Pu distribution ... 53
Figure 23 Comparison of combined resistances in uneven and even configurations ... 55
Figure 24 Schematic drawing of thermal resistances connected in series and parallel ... 57
Figure 25 Ternary Pu concentration map divided into four sections for evaluation of thermal resistivity of MIMAS-MOX fuel with 8.4 % Pu ... 59
Figure 26 Ternary Pu concentration map divided into four sections for evaluation of thermal resistivity of MIMAS-MOX fuel with 14.3 % Pu ... 64
Figure 27 Comparison of prediction with measurements on thermal conductivity of MOX fuel with homogeneous and heterogeneous Pu distributions ... 66
Figure 28 Effect of fission products on thermal resistivity as a function of burnup ... 69
Figure 29 Comparison of prediction with measurements on thermal conductivity of MOX fuel with homogeneous and heterogeneous Pu distributions with the identical Pu content and burnup ... 70

1. Introduction

Mixed oxide (MOX) fuel, composed of plutonium (Pu) and uranium (U), is used in light water reactors for effective use of uranium resources. The current commercial MOX fuel is fabricated via the micronized master blend (MIMAS) process for mixing plutonium oxide (PuO_2) and uranium oxide (UO_2) powders. It is known that the MOX fuel fabricated via the MIMAS process exhibits a heterogeneous microstructure characterized by agglomerates with higher Pu concentrations compared to the surrounding fuel matrix [1][2][3]. The heterogeneous distribution of Pu in MIMAS–MOX fuel can influence its properties and behaviors. To address this, the author conducted a comprehensive research project to investigate the fuel properties and behaviors of MIMAS–MOX fuel. The primary results of this project, including thermal conductivity measurements of unirradiated and irradiated MIMAS–MOX fuel, have been published [1]. Thermal conductivity is an important fuel property because most fuel properties and behaviors are temperature dependent. Accordingly, the thermal conductivity of MIMAS–MOX fuel has been the subject of numerous studies [1][4][5][6][7][8][9][10][11][12][13][14]. In some of the studies [1][7][11][14], irradiated heterogeneous MOX fuels fabricated via the MIMAS process and other process than MIMAS exhibited higher thermal conductivity than irradiated homogeneous MOX fuels fabricated via the short binderless route (SBR) process for powder mixing. However, the influence of heterogeneous Pu distribution on thermal conductivity is not yet fully understood or modeled. The objectives of this study are to explain the mechanism how the heterogeneous Pu distribution gives an effect on the overall thermal conductivity and to formulate its effect.

Initially, experimental investigations were conducted on the thermal conductivity of single crystalline UO_2 and polycrystalline UO_2 in unirradiated state. These results provided a foundational basis of understanding and formulating the thermal conductivity of MIMAS-MOX fuel. This is presented in Chapter 2, following this introduction of Chapter 1.

Next, detailed observations were performed on both unirradiated and irradiated MIMAS-MOX fuels to examine the distributions of Pu, which acts as an impurity element to

decrease the thermal conductivity. Thermal conductivity measurements were then carried out using the laser flash method on unirradiated and irradiated MIMAS-MOX fuels as well as on references of UO_2 fuel and SBR-MOX fuel. These results are shown in Chapter 3.

Finally, the thermal conductivity of MIMAS-MOX fuel was discussed and modeled based on results of the study mentioned above. In the discussion, thermal resistivity was focused on rather than thermal conductivity in order to facilitate understanding of the effects of heterogeneous Pu distribution, as Pu atoms behave as resistance against thermal flow. First, the effects of Pu content and also burnup on the thermal resistivity of homogeneous MOX fuel were investigated. Subsequently, the effect of heterogeneous Pu distribution was analyzed using the concept of thermal resistance circuits. As a result, a model formula was proposed to estimate the thermal conductivity of unirradiated and irradiated MIMAS–MOX fuels considering the heterogeneous Pu distribution. This model successfully explains the mechanism how the heterogeneous Pu distribution affect the thermal conductivity. These are shown in Chapter 4.

2. Thermal conductivity measurements for single crystalline and polycrystalline UO_2

This chapter presents measurements of the thermal conductivity of single crystalline UO_2 and polycrystalline UO_2 in unirradiated state. The results of this experimental measurement become a fundamental basis of understanding and formulating the thermal conductivity of MIMAS-MOX fuel. The contents of this chapter are published in the paper [15] of the author.

2-1 Material

Thermal conductivity measurements were performed on both single-crystalline and polycrystalline UO_2 specimens. The single-crystalline sample was a (100)-oriented rectangular plate with a thickness of 1 mm. For the polycrystalline specimens, UO_2 powder served as the starting material. The powder was heat-treated in a 4% H_2-Ar atmosphere at 600°C for 2 hours to achieve an oxygen-to-uranium (O/U) ratio of 2.0. Subsequently, the powder was homogenized using an agate mortar, cold-pressed into pellets, and subjected to a solid-state reaction at 1600°C for 72 hours in the same reducing atmosphere. Following the solid-state reaction, the resulting UO_2 samples were manually ground and further granulated via wet ball milling. The granulated powder was loaded into a graphite die and densified by spark plasma sintering (SPS-515S, Sumitomo Coal Mining Co.) under an argon flow. Sintering was conducted at 1500°C for 10 minutes under an applied pressure of 50 MPa. Finally, the sintered specimens were heated in an electric furnace at 1200°C for 5 hours in a 4% H_2-Ar atmosphere to adjust the O/U ratio.

2-2 Method

2-2-1 Sample observation

The crystal structures of the prepared samples were characterized by X-ray diffraction (XRD) using a Rigaku Ultima IV diffractometer equipped with a Cu-Kα radiation source. Diffraction data were collected over a 2θ range of 20–120°. The obtained XRD patterns were

externally calibrated using silicon (Si) standards to determine the lattice parameters. Sample density was calculated based on the measured dimensions and mass, while the relative density was derived from the lattice constants. The grain morphology of the polycrystalline UO_2 specimens was examined by electron backscatter diffraction (EBSD) in conjunction with field-emission scanning electron microscopy (FE-SEM; JEOL, JSM-6500F).

2-2-2 Method of thermal conductivity measurement

Thermal diffusivity was measured using the laser flash method with a thermal constants analyzer (LFA 457, NETZSCH) over the temperature range from room temperature to 1173 K. In this study, the thermal diffusivity was evaluated using the half-time method. The Cowan correction was used to correct for heat loss from the surface of the sample. Based on the measured thermal diffusivity $\alpha(T)$, specific heat $C_p(T)$, and sample density $\rho(T)$, the thermal conductivity $k(T)$ was calculated using Equation (1). For the specific heat capacity of UO_2, the value in [17] was employed.

$$\boldsymbol{k(T) = \alpha(T) \cdot C_p(T) \cdot \rho(T)} \quad (1)$$

All the samples had sufficiently densities with values ranging from 94% to 99% of the theoretical density. To account for the porosity-related discrepancy, the thermal conductivity values were corrected to 100% theoretical density using the Maxwell-Eucken equation [18][19] as shown in Equation (2)

$$\boldsymbol{k_{100}(T) = k_p(T) \cdot \frac{1 + \beta p}{1 - p}} \quad (2)$$

In this equation, $k_{100}(T)$ represents the thermal conductivity at full theoretical density, $k_p(T)$ denotes the thermal conductivity at a porosity volume fraction p, and β is a shape-dependent constant. In this study, a value of 0.5 was used for β, which is applicable to spherical pores.

2-3 Results

2-3-1 Results of sample observation

Figure 1 presents the X-ray diffraction (XRD) patterns of both single-crystalline and polycrystalline UO_2 samples, along with the pair distribution function (PDF) of UO_2. The diffraction peaks observed for the single-crystalline UO_2 are consistent with the (100) reflections in the PDF, confirming the crystal orientation. No impurity peaks were detected in any of the XRD patterns, indicating that all samples were single-phase with a fluorite-type crystal structure.

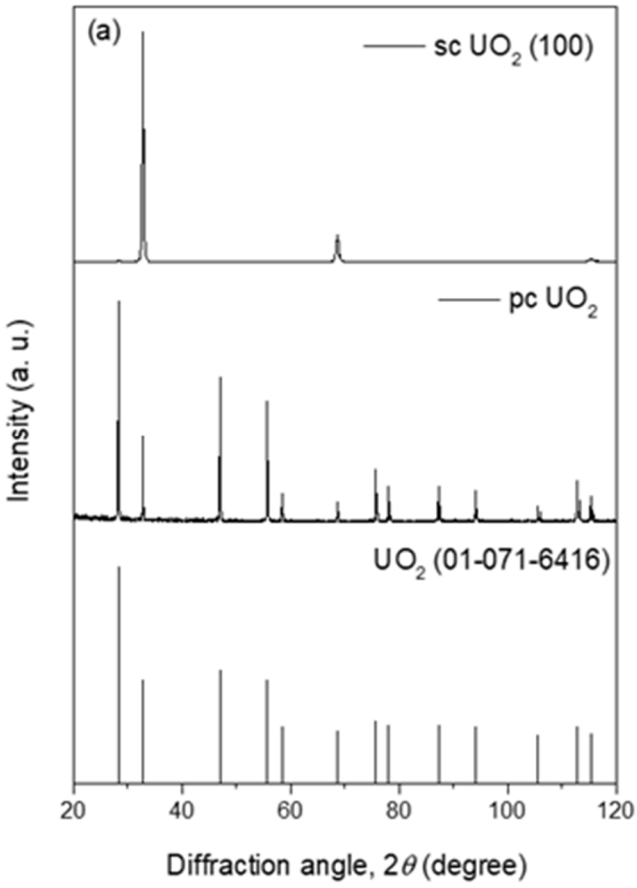


Figure 1　XRD patterns of single crystalline (sc) and polycrystalline (pc) UO_2

Table 1 summarizes the lattice constants and densities in ratio to theoretical density derived from the XRD measurements. The sample exhibited a density exceeding 95% of the theoretical density.

Table 1 Characteristics of fabricated samples

Sample	Lattice constant a (nm)	Relative density (%T.D.)
Single crystalline UO_2	-	-
Polycrystalline UO_2	0.5471	96.22

Figure 2 displays the inverse pole figure (IPF) map obtained from electron backscatter diffraction (EBSD) analysis of polycrystalline UO_2. The grain orientations appear to be nearly random, indicating that the influence of spark plasma sintering (SPS), a pressure-assisted sintering technique, on texture development is negligible. The average grain size, calculated based on the area of individual grains, was approximately 10 μm.

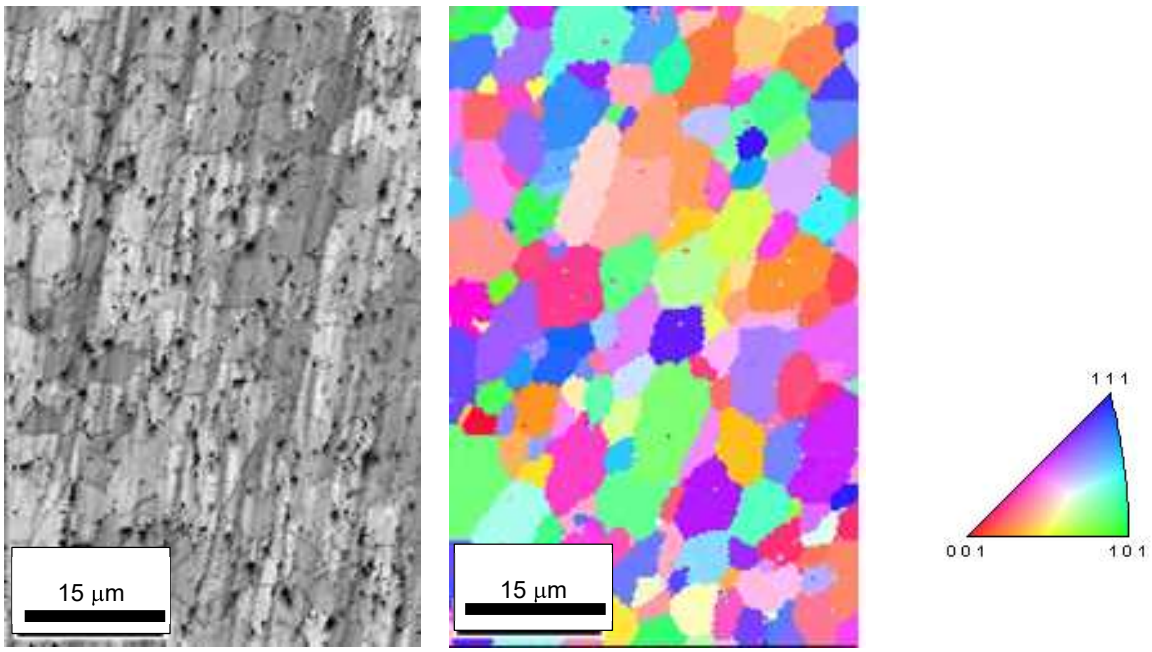


Figure 2 EBSD image of polycrystalline UO_2 (2000x)

2-3-2 Results of thermal conductivity measurement

The measured thermal conductivities of single-crystalline and polycrystalline UO_2 are presented in Figure 3 [15], along with previously reported values [16][20][21][22][23][24][25]. Notably, the reported thermal conductivities of single-crystalline UO_2 exhibit considerable

variation at low temperatures, which may be attributed to the presence of small amount of impurities in the samples.

The thermal conductivity of the single-crystalline UO_2 measured in this study closely matches the values reported by Bates and is relatively higher than those in other studies. This suggests that the impurity content in the single crystalline UO_2 samples used in this study was small.

For polycrystalline UO_2, the measured thermal conductivity is nearly identical to that of the single-crystalline UO_2 obtained in this study. A similar trend is observed in the data reported by Moore [21], as shown in Figure 3.

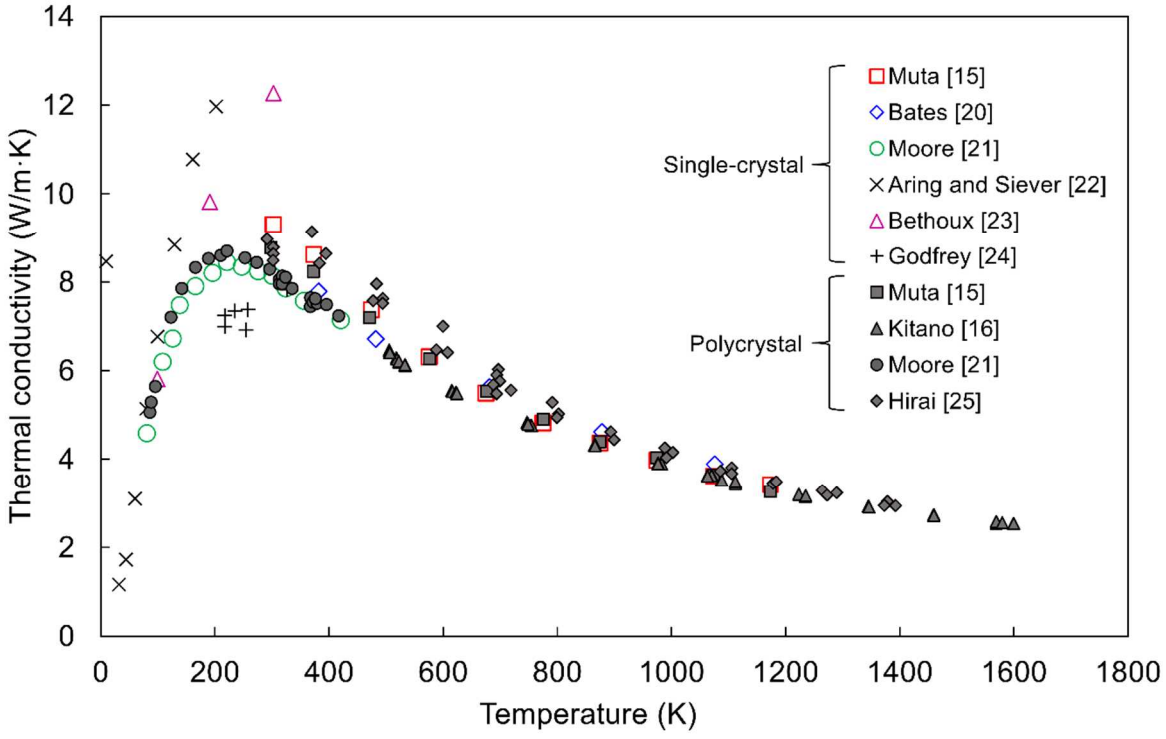


Figure 3 Thermal conductivity of single crystalline and polycrystalline UO_2 with a theoretical density of 100 % [15]

2-4 Discussion

2-4-1 Application of the results to thermal conductivity of MOX fuel

For use in the subsequent chapters, the thermal conductivity measurements for polycrystalline UO_2 reported in [15][16] , as shown in Figure 3, were corrected to the values for 95% of the theoretical density (TD), since most thermal conductivity models employed in fuel design and safety assessments are standardized to 95% TD [26]. These corrected values were then converted to thermal resistivity by taking their reciprocal. Figure 4 illustrates the thermal resistivity as a function of temperature. In the temperature range where phonon conduction dominates the heat transport mechanism, the thermal resistivity exhibits a linear dependence on temperature [27].

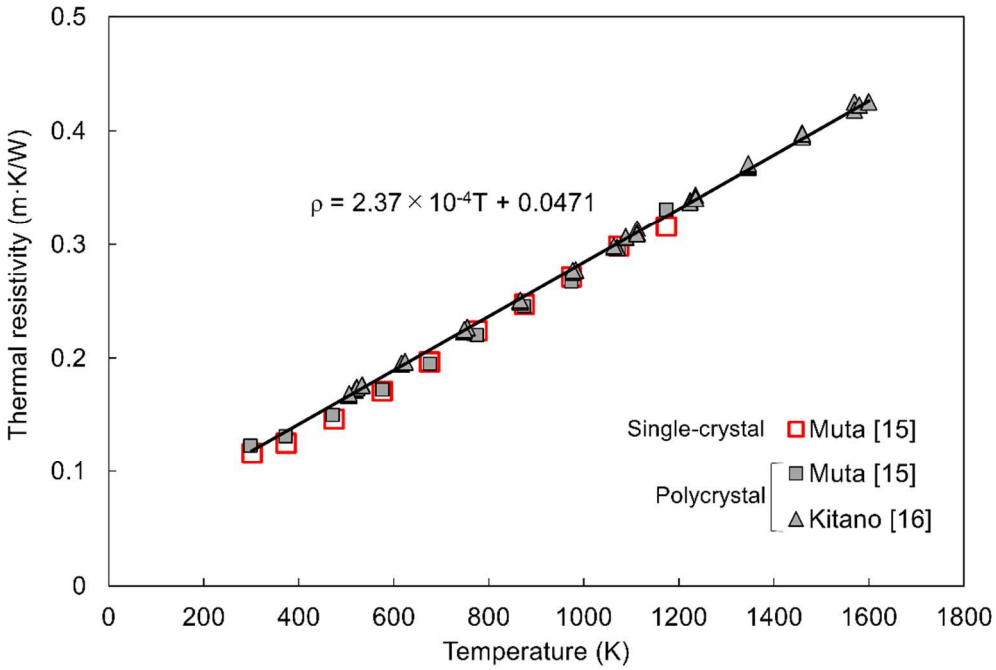


Figure 4 Thermal resistivity of unirradiated single-crystalline and polycrystalline UO_2 with a theoretical density of 95 %

As shown in Figure 4, the thermal resistivity of unirradiated polycrystalline UO_2, based on the data reported in [15][16] can be approximated by Equation (3) which serves as a foundational model for formulating the thermal resistivity or thermal conductivity of MOX fuels with both homogeneous and heterogeneous plutonium distributions:

$$\rho_{\mathrm{unirr_{UO2}}} = 2.37 \times 10^{-4} T + 0.0471 \quad [\mathrm{m \cdot K/W}] \tag{3}$$

Another finding from Figure 3 is that the measured thermal conductivity of the polycrystalline UO_2 is nearly identical to that of the single-crystalline UO_2. This indicates that the effect of grain boundary on phonon scattering is negligible for UO_2 with grain size of 10 μm or larger. Figure 5 shows the values of thermal conductivity, k calculated from the following equations, where C_{ph} is the phonon specific heat, v_{s} is the phonon velocity, ω is the phonon frequency, τ is the relaxation time and l_{GB} is grain size. The subscripts imp, def, gb, and u in the relaxation time denotes impurity atoms, lattice defects, grain boundaries, and phonon-to-phonon interactions (Umklapp process) respectively. The parameters of $\alpha_1 = 0.72$ and $\beta_1 = 0.7$, which are recommended as scattering parameters in [28] were used for the calculation [15].

$$k = \int_0^{\omega_{max}} C_{\mathrm{ph}} \cdot {v_{\mathrm{s}}}^2 \cdot \tau d\omega$$

$$\frac{1}{\tau} = \frac{1}{\tau_{\mathrm{imp}}} + \frac{1}{\tau_{\mathrm{def}}} + \frac{1}{\tau_{gb}} + \frac{1}{\tau_{\mathrm{u}}} + \cdots\cdots$$

$$\frac{1}{\tau_{gb}} = \frac{v_{\mathrm{s}}}{\alpha_1 \cdot l_{\mathrm{GB}} \cdot \beta_1 \cdot \frac{\omega_0}{\omega}}$$

In Figure 5, the effect of grain boundary scattering on thermal conductivity appears to be sufficiently weak that it can be considered negligible for grain sizes ranging from 1 μm to 100 μm, particularly at 500 K and 1000 K, which are within the typical operating temperature range of light water reactors. This observation supports the measurements for UO_2 shown in Figure 3.

In MOX fuel, i.e., $(U,Pu)O_2$, uranium atoms at the cation sites are partially replaced by plutonium atoms. Grain boundaries are interfaces between crystal grains characterized by mismatched atomic arrangements. Since the substitution of uranium atoms with plutonium atoms does not change the nature of atomic disorder at these interfaces, phonon scattering at

grain boundaries is expected to remain unaffected. Therefore, it is reasonable to assume that grain boundary effects on thermal conductivity are negligible in MOX fuel as well.

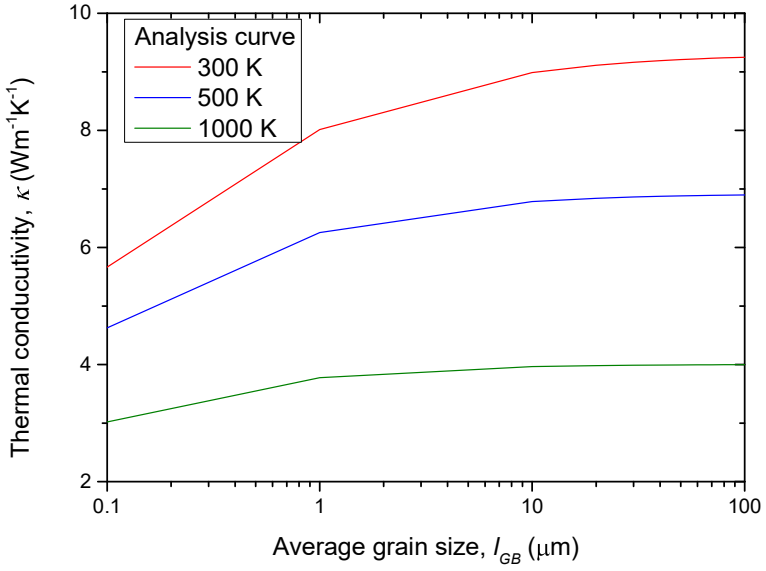


Figure 5 Grain size dependence of thermal conductivity at 300 K, 500 K, and 1000 K for UO_2

3. Thermal conductivity measurement for unirradiated and irradiated MOX fuels

This chapter presents thermal conductivity measurements of MIMAS-MOX and SBR-MOX fuels, along with a reference sample of UO_2 fuel, under both unirradiated and irradiated conditions. Microstructural observations obtained through electron probe microanalysis (EPMA) and electron backscatter diffraction (EBSD) are also included. The formulation of the thermal conductivity model for MIMAS-MOX fuel in Chapter 4 is based on the experimental results described in this chapter. The contents are derived from the author's previously published works [1][16][29][30].

3-1 Material

3-1-1 Sampled fuels

(a) Fuel Specification at fabrication

Two types of MOX fuel were fabricated for irradiation testing in the Halden reactor, along with UO_2 fuel used as a reference. One of the MOX fuels was fabricated via the SBR process for powder mixing in the United Kingdom. The SBR-MOX fuel exhibits a microstructure characterized by a homogeneous plutonium distribution. The other MOX fuel was fabricated using the MIMAS process for powder mixing in France, resulting in a microstructure with heterogeneous plutonium distribution. The UO_2 fuel was manufactured at the Kjeller laboratory of the Institute for Energy Technology (IFE) in Norway. Table 2 summarizes the specifications of the three fuel types.

Another MIMAS-MOX fuel was fabricated in Belgium for irradiation testing, initially in the BR3 reactor and subsequently in the BR2 reactor. Table 3 provides specifications of the MIMAS-MOX fuel.

Table 2 Specifications of the fuel rods irradiated in the Halden reactor [31]

Fuel type	SBR-MOX	MIMAS-MOX	UO_2
Producer	BNFL	CEA	IFE
Synthesis route	SBR	MIMAS	-
Initial Pu-fissile content (%)	6.1	6.1	-
Initial Pu content (%)	8.4	8.4	-
Initial U-235 enrichment (%)	depleted	depleted	8.0
O/M ratio	1.979	2.023	2.021
Density (%TD)	95	95	95

Table 3 Specifications of the fuel rods irradiated in the BR3 and BR2 reactor [32]

Fuel type	MIMAS-MOX
Producer	Belgonucleaire N. V.
Synthesis route	MIMAS
Initial Pu-fissile content (%)	10.1
Initial Pu content (%)	14.3
Initial U-235 enrichment (%)	depleted
O/M ratio	1.989
Density (%TD)	93.5

(b) Irradiation

An irradiation test for the three fuels in Table 2 was performed in the Halden reactor that was a heavy water cooled and moderated research reactor in Norway. During the irradiation test, the coolant temperature ranged from 506 to 508 K, and the coolant pressure was maintained between 2.8 and 2.9 MPa. The average fast neutron flux reached a maximum of 2.0×10^{13} cm^{-2} s^{-1}. Table 4 [31] lists the discharged burnups of the fuel rods assessed from the results of the axial gamma scanning after the irradiation.

Table 4 Fuel rod burnups after the irradiation test at the Halden reactor [31]

Fuel type	SBR-MOX	MIMAS-MOX	UO_2
Axial rod-average burnup (GWd/t)	70.0	69.4	69.1
Axial rod-peak burnup (GWd/t)	74.4	73.8	73.5

Another irradiation test was conducted at the BR2 reactor in Belgium for the two fuel rods of MIMAS-MOX fuel containing 14.3% plutonium, as specified in Table 3. Table 5 summarizes the discharged burnup values of the fuel rods, which were determined from axial gamma scanning performed after irradiation.

During the irradiation, the average coolant temperature was 562 K at the inlet and 576 K at the outlet. The coolant pressure was maintained at 15.5 MPa, and the maximum axially averaged fast neutron flux was approximately $3.0 \times 10^{13}\ \mathrm{cm^{-2}s^{-1}}$.

Table 5 Fuel rod burnup after the irradiation test at the BR2 reactor [16]

Fuel type	MIMAS-MOX	
Rod ID	F6673	F6677
Axial rod-average burnup (GWd/t)	24.3	35.7
Axial rod-peak burnup (GWd/t)	34.9	53.7

3-1-2 Samples for thermal conductivity measurement

The samples subjected to the thermal conductivity measurement are listed in Table 6. Four samples were obtained from the unirradiated fuels specified in Table 2 and Table 3. Three samples were obtained from the fuel rods irradiated in the Halden reactor listed in Table 4, and two samples were obtained from the fuel rods irradiated in the BR2 reactor in Table 5.

Table 6 Samples subjected to thermal conductivity measurement [16]

Fuel type	Initial Pu content (%)	Reactor used for irradiation	Sample burnup (GWd/t)	Sample density (g/cm^3)
UO_2	0	(unirradiated)	0	10.52
SBR-MOX	8.4	(unirradiated)	0	10.40
MIMAS-MOX	8.4	(unirradiated)	0	10.41
MIMAS-MOX	14.3	(unirradiated)	0	10.28
UO_2	0	Halden	72	9.99
SBR-MOX	8.4	Halden	68	9.79
MIMAS-MOX	8.4	Halden	68	9.86
MIMAS-MOX	14.3	BR2	34	10.50
MIMAS-MOX	14.3	BR2	50	10.38

3-2 Method

3-2-1 Sample observation

(a) Observations on unirradiated MIMAS-MOX fuels

To characterize the heterogeneous Pu distribution, the two kinds of unirradiated MIMAS-MOX fuels with initial Pu contents of 8.4 % and 14.3 % (hereinafter simply called 8.4 % Pu and 14.3% Pu) were examined using EPMA and EBSD. Sample preparation and observation using EPMA and EBSD were performed at the hot laboratory of SCK-CEN in Belgium. EPMA analysis was performed using a CAMECA SX100R instrument configured with an accelerating voltage of 15 kV, a probe current of 100 nA, a beam diameter of <1 μm, a step size of 0.3 μm, and a dwell time of 35 ms. The relative uncertainty in quantitative EPMA analysis was approximately 1% [33]. EBSD analysis was carried out using an FEI SCIOS system equipped with an EDAX EBSD detector. The operating conditions included an accelerating voltage of 20 kV, a sample tilt angle of 70°, a probe current of 2 nA, a step size of 0.2 μm, and a dwell time of 8 ms. Further details regarding the EPMA and EBSD

instrumentation and measurement conditions are provided in a publication authored by SCK-CEN who is the operator responsible for these observations [34].

The crystal grain size was evaluated through image analysis of crystal grain maps via EBSD. Two methods were employed to measure crystal grain size: the lineal intercept length (IL) method and equivalent circular diameter (ECD) method. In the IL method, straight lines evenly spaced in the four directions (0°, 45°, 90°, 135°) were used to intercept crystal grains, following the guidelines of ASTM E1382 [35], in order to minimize the influence of preferential orientation. In the ECD method, each crystal grain was geometrically transferred into a circle with an equivalent area, and the diameter of this circle was measured as the ECD. Both IL and ECD represent crystal grain sizes on the cross-sectional plane. When estimating the volumetric diameter of three-dimensional crystal grain, a correction factor such as 1.571 recommended in ASTM E112-10 [36] must be multiplied.

(b) Observations on irradiated fuels

Optical microscopy was performed on the cross-section of the five irradiated fuel rods listed in Table 4 and Table 5.

Elemental analysis for the SBR-MOX and MIMAS-MOX fuels irradiated in the Halden reactor was performed using a CAMECA SX100R EPMA instrument at the Cadarache site of CEA in France. The EPMA was operated with a probe current of 200 nA and a beam size of 1 μm. Surface analysis of Pu distribution was performed at the three different radial positions with an accelerating voltage of 30 kV. Line scanning for a fission product of neodymium in the MIMAS-MOX fuel was performed from the center to the periphery with an accelerating voltage of 20 kV.

For the MIMAS-MOX fuels irradiated in the BR2 reactor, EPMA observation were conducted using a CAMEBAX-R instrument at the Mol site of SCK-CEN in Belgium. The EPMA was operated with an accelerating voltage of 20 kV, a probe current of 100 nA, and a dwell time of 17−19 ms. Surface analysis of Pu distribution was performed from the center to

the periphery. Line scanning for fission products, including neodymium, was performed across a Pu-rich agglomerate.

3-2-2 Method of thermal conductivity measurement

(a) Sample preparation for thermal diffusivity measurement by laser flash method

For the unirradiated samples, a 1 mm-thick disc was sliced out from the fuel pellet and used for thermal diffusivity measurement. For the irradiated samples, a 1 mm-thick disc fractured into several pieces during slicing work due to pre-existing cracks in the fuel pellet. A key requirement for thermal diffusivity measurement is a flat specimen of sufficient thickness, as the method assumes one-dimensional heat flow between the top and bottom surfaces. Accordingly, a fragment of the disc that possessed flat surfaces and a volume large enough to satisfy the planar geometry assumption was selected for measurement.

(b) Conversion of thermal diffusivity to thermal conductivity

The thermal conductivity $k(T)$ was calculated using Equation (1) presented in Chapter 1. In this measurement, the thermal diffusivity $a(T)$ was measured with a laser flash apparatus installed in a lead-shielded glove box at JRC Karlsruhe in Germany. The measurement procedure followed the same methodology as described in references [11][37]. The specific heat $C_p(T)$ was determined by differential scanning calorimetry for the unirradiated samples. For the irradiated samples, the specific heat was assumed to be equivalent to that of the unirradiated samples, as reported in reference [4]. Density $\rho(T)$ was measured at room temperature using the immersion technique. Temperature dependence of the density was calculated using the temperature dependence as recommended in [38]. All thermal conductivity values derived from Equation (1) were corrected to those for a typical theoretical density ratio of 95 % using Equation (4) to enable comparison with published data. Considering the relative uncertainties on the thermal diffusivity, specific heat and density, the overall relative uncertainty in the thermal conductivity is estimated to be approximately 10% [11][37].

$$k_{95}(T)=\frac{1-0.05f(T)}{1-p\cdot f(T)}k(T) \quad (4)$$

where $f(T)$ = 2.6-0.5 (T-273.15)/1000. p is the porosity fractional volume. T is the absolute temperature in Kelvin.

(c) Measurement procedure

The thermal diffusivity for the irradiated samples was measured under thermal cycles involving temperature-ascent and temperature-descent processes. In each cycle, the target temperature was increased by approximately 100 K, starting from 540 K. This procedure was adopted to mitigate the risk of sample fracture due to thermal stress. For the irradiated UO_2 fuel sample, measurements were successfully performed up to the ninth cycle, reaching temperatures of approximately 1400 K. In contrast, the irradiated MOX fuel samples fractured during the fifth cycle, at temperatures between 920 K and 950 K, despite the precautions taken. Consequently, measurements above 950 K could not be obtained for the irradiated MOX samples.

The thermal diffusivity values obtained during the thermal cycles around the reaching temperature of 1000 K are considered representative of the actual thermal diffusivity as typical fuel temperatures during commercial reactor operation are around 1000 K. Therefore, the data from the fifth cycle were adopted for both irradiated UO_2 and MOX fuels in the discussion of thermal conductivity.

Figure 6 presents an example of thermal conductivity values derived from experimental measurements of thermal diffusivity under thermal cycling on a MIMAS-MOX sample irradiated up to 68 GWd/t. The results indicate that thermal conductivity increases with the maximum temperature reached in each cycle, which is attributed to the annealing effect.

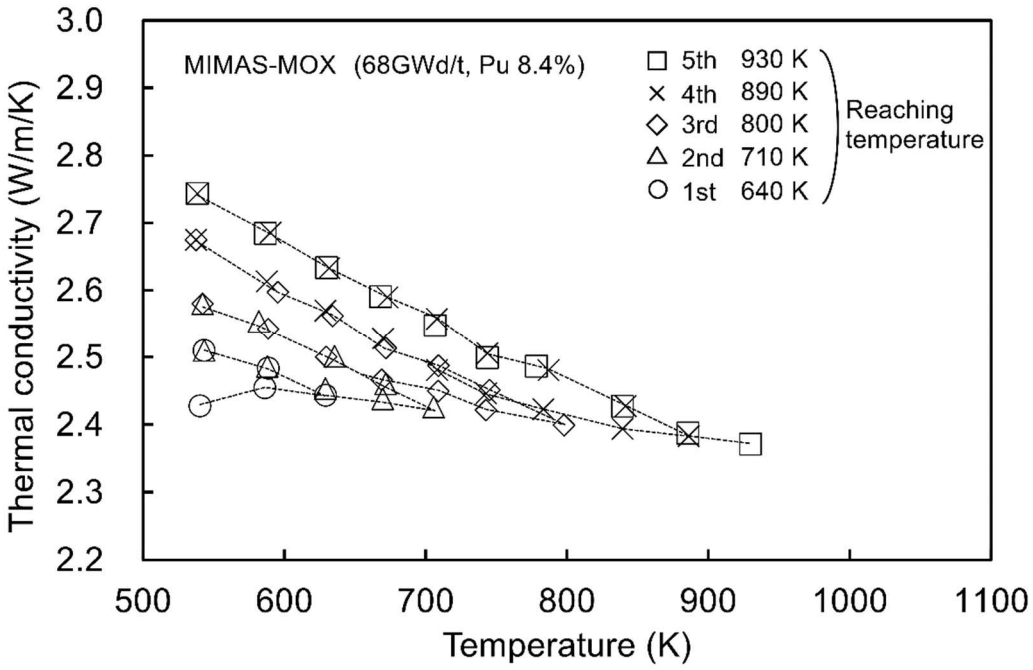


Figure 6 Thermal conductivities converted from thermal diffusivities measured under thermal cycles [1]

3-3 Results

3-3-1 Results of sample observation

(a) Observations on unirradiated MIMAS-MOX fuels

Results of the observation on the unirradiated MIMAS-MOX fuels with 8.4 % Pu and 14.3 % Pu using EPMA and EBSD are shown in Figure 7 and Figure 8. In both figures, EPMA and EBSD images are overlapped. Accordingly, they show both Pu distribution and grain boundaries within one image.

Figure 7 illustrates Pu-rich agglomerates with around 25% Pu (green area), intermediate phase with around 7% Pu (blue area), and U agglomerates with little Pu (magenta area) in the MIMAS-MOX fuel with 8.4 % Pu. The gray portions correspond to pores. Grain boundaries appear as a net-like pattern in the colored phases. The crystal grains in the Pu-rich agglomerates appear larger than those in the intermediate phase and the U agglomerates in Figure 7.

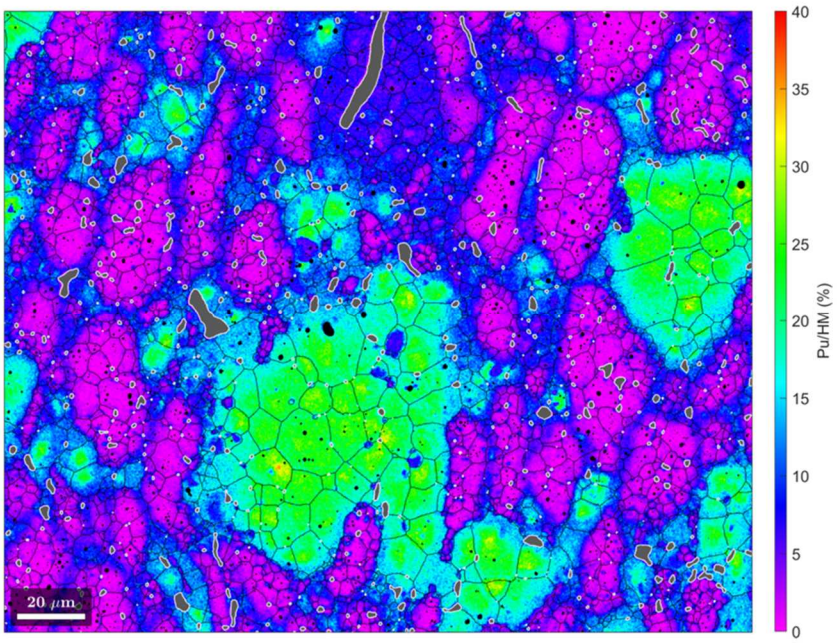


Figure 7 Overlapped image from the EPMA and EBSD on the MIMAS-MOX fuel 8.4 % Pu [30]

Figure 8 presents Pu-rich agglomerates with more than 25% Pu (green - red area) and U agglomerates with little Pu (magenta area) in the MIMAS-MOX fuel with 14.3 % Pu. The intermediate phase with around 7% Pu (blue area) appears as a thin shell surrounding the U agglomerates. Compared to Figure 7, the Pu-rich agglomerates in Figure 8 exhibit smaller crystal grains and contain elevated Pu concentrations approaching 40% (red areas).

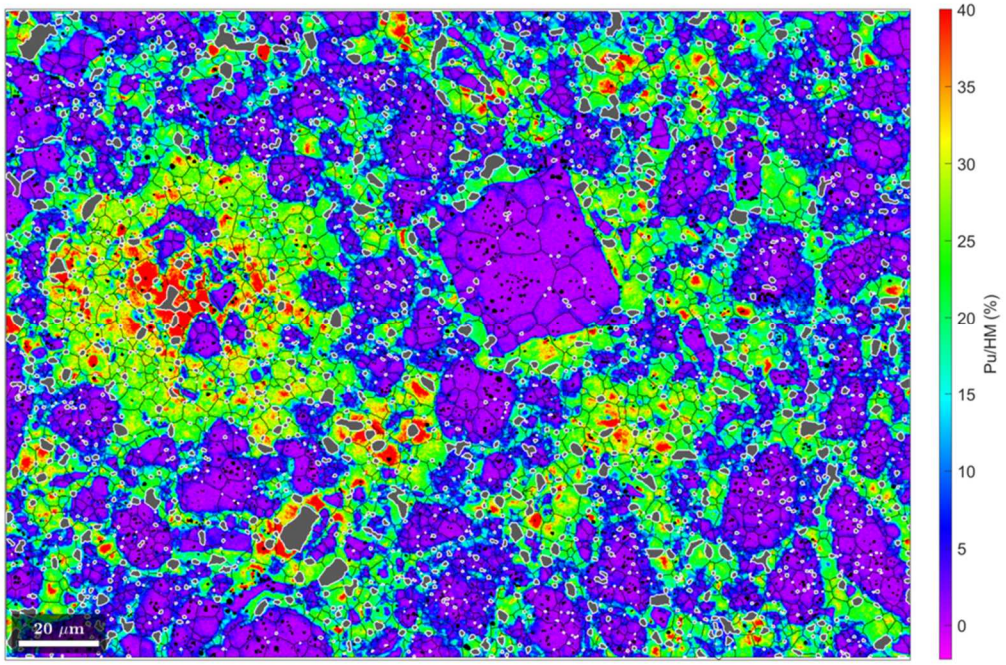


Figure 8 Overlapped image from the EPMA and EBSD on the MIMAS-MOX fuel with 14.3 % Pu [30]

Figure 7 and Figure 8 were processed into ternary phase maps as shown in Figure 9 and Figure 10, for the unirradiated MIMAS-MOX fuels with nominal Pu contents of 8.4% and 14.3%, respectively. Each map shows three distinct regions: U agglomerates (red), intermediate phase (blue), and Pu-rich agglomerates (green). In this study, the Pu concentration ranges were defined as follows:

For the MIMAS-MOX fuel with 8.4% Pu:

- U agglomerates: 0% ≤ Pu < 4%
- Intermediate phase: 4% ≤ Pu < 12%
- Pu-rich agglomerates: Pu ≥ 12%

For the MIMAS-MOX fuel with 14.3% Pu:

- U agglomerates: 0% ≤ Pu < 4%
- Intermediate phase: 4% ≤ Pu < 15%
- Pu-rich agglomerates: Pu ≥ 15%

It is important to note that different threshold values (12% and 15%) were applied to distinguish between the intermediate phase and Pu-rich agglomerates in the two fuel types, reflecting their respective total Pu contents.

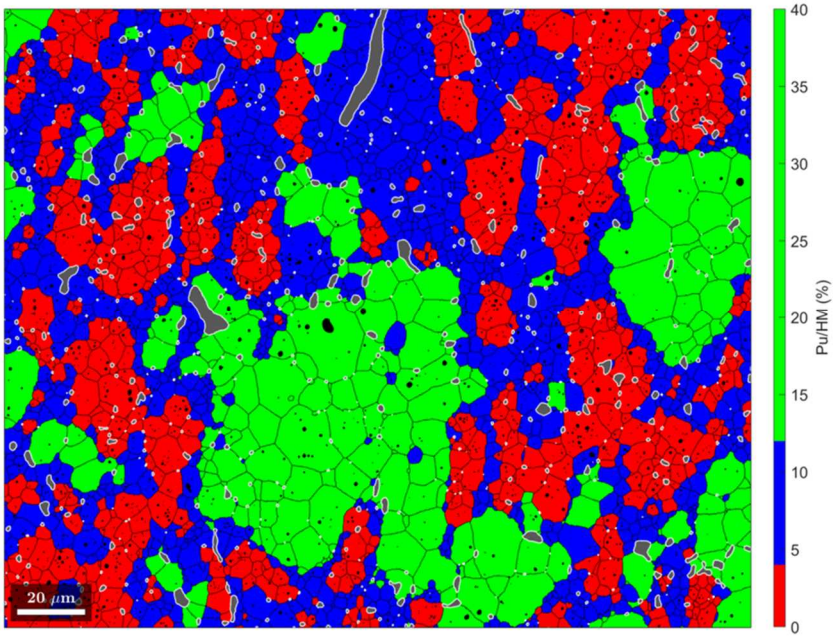


Figure 9 Ternary phase map consisting of the U agglomerate, intermediate phase, and Pu-rich agglomerate on the MIMAS-MOX fuel with 8.4 % Pu [30]

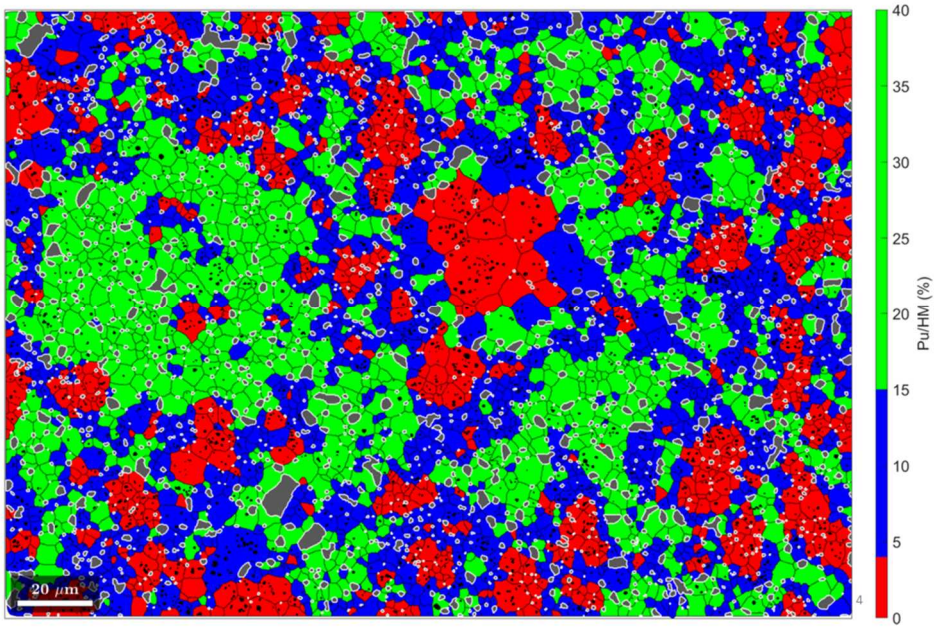


Figure 10 Ternary phase map consisting of the U agglomerate, intermediate phase, and Pu-rich agglomerate on the MIMAS-MOX fuel with 14.3 % Pu [30]

A total of four ternary maps including Figure 9 for the MIMAS-MOX fuel with 8.4 % Pu were subjected to image analysis to quantify the area fractions of the three phases and to evaluate crystal grain sizes. An identical analysis was performed for the MIMAS-MOX fuel with 14.3 % Pu. The results are summarized in Table 7 and Table 8, respectively. The definitions of crystal grain size in Table 7 and Table 8 are as follows.

$$IL\ (\text{average}) = \frac{\sum_{i=1}^{N} IL_i}{N}, \qquad N: Total\ number\ of ILs$$

$$IL\ (\text{D50}) = IL_n, \qquad where\ \ \frac{\sum_{i=1}^{n} IL_i}{\sum_{i=1}^{N} IL_i} = 0.5, \qquad IL_i \le IL_{i+1}$$

$$ECD\ (\text{average}) = \frac{\sum_{i=1}^{N} ECD_i}{N}, \qquad N: Total\ number\ of ECDs$$

$$ECD\ (\text{D50}) = ECD_n, \qquad where\ \ \frac{\sum_{i=1}^{n} ECD_i}{\sum_{i=1}^{N} ECD_i} = 0.5, \qquad ECD_i \le ECD_{i+1}$$

As shown in Table 7, the three phases in the MIMAS-MOX fuel with 8.4 % Pu occupy nearly equal area fractions. Among them, the intermediate phase contains the highest number of crystal grains, as indicated by the total count of ECDs. When comparing the average crystal grain size and the D50 value, the D50 is consistently larger. This trend is particularly pronounced in the Pu-rich agglomerates. The measured ILs and ECDs across all maps range from 3.7μm to 5.6 μm, suggesting that the choice of evaluation method significantly influences the results and cannot be disregarded.

The average Pu concentration across the four maps is 9.47%, which exceeds the nominal Pu content of 8.4% listed in Table 2. This indicates that the selected maps for image analysis contained a higher proportion of Pu-rich agglomerates than the bulk average. The ratios of Pu concentration relative to the overall average of 9.47% are 0.23 for the U agglomerates, 0.79 for the intermediate phase, and 1.86 for the Pu-rich agglomerates. Given that local burnup is proportional to Pu concentration, the expected burnup ratios for these three phases are

approximately 0.23, 0.79, and 1.86, respectively.

Table 7 Statistical data of the measurements via EPMA and EBSD on the MIMAS-MOX fuel with 8.4 % Pu [30]

Sample	Item of data	All four maps	U agglomerate	Intermediate phase	Pu-rich agglomerate
8.4 % Pu MIMAS-MOX	Area fraction	-	0.31	0.34	0.35
	Average Pu [%]	9.47	2.19	7.50	17.65
	Ratio to average Pu for all four zones	1	0.23	0.79	1.86
	Total number of ILs	11499	3700	5294	2505
	IL (average) [μm]	4.4	4.2	3.2	7.0
	IL (D50) [μm]	5.6	5.1	3.8	9.1
	Total number of ECDs	9410	2723	5544	1143
	ECD (average) [μm]	3.7	4.0	2.9	6.4
	ECD (D50) [μm]	4.4	4.6	3.3	9.0

As shown in Table 8, the intermediate phase and Pu-rich agglomerates occupy larger area fractions compared to the U agglomerates in the MIMAS-MOX fuel containing 14.3% Pu. Unlike the observations in the 8.4% Pu fuel, the average crystal grain sizes and the D50 values agree. The measured ILs and ECDs across all maps range narrowly from 2.9 μm to 3.2 μm, and the values show good agreement. These results indicate that, for the MIMAS-MOX fuel with 14.3 % Pu, the evaluation method has minimal influence on the grain size assessment. The ratios of Pu concentration relative to the overall average of 12.66% are 0.18 for the U agglomerates, 0.67 for the intermediate phase, and 1.85 for the Pu-rich agglomerates. Given the proportional relationship between local burnup and Pu concentration, the expected burnup ratios for these three phases are approximately 0.18, 0.67, and 1.85, respectively.

Table 8 Statistical data of the measurements via EPMA and EBSD on the MIMAS-MOX fuel with 14.3 % Pu [30]

Sample	Item of data	All four maps	U agglomerate	Intermediate phase	Pu-rich agglomerate
14.3 % Pu MIMAS-MOX	Area fraction	-	0.23	0.40	0.37
	Average Pu [%]	12.66	2.33	8.51	23.46
	Ratio to entire average Pu	1	0.18	0.67	1.85
	Total number of ILs	15982	3314	7101	5567
	IL (average) [μm]	2.9	3.2	2.5	3.2
	IL(D50) [μm]	3.2	3.6	2.6	3.6
	Total number of ECDs	14228	2781	7144	4303
	ECD (average) [μm]	3.1	3.3	2.8	3.5
	ECD(D50) [μm]	3.0	3.2	2.6	3.6

(b) Observations on irradiated fuels

Figure 11 presents ceramographic images obtained via optical microscopy from cross-sections of five irradiated fuel rods, as listed in Table 4 and Table 5. The burnup values indicated in Figure 11 correspond to the pellet-average burnup at the sample position.

In the three MIMAS-MOX fuel samples, distinct black spots are observed, which correspond to Pu-rich agglomerates. When comparing the MIMAS-MOX fuel irradiated to 72.8 GWd/t with the SBR-MOX fuel irradiated to 73.2 GWd/t, the microstructural changes are more pronounced in the MIMAS-MOX fuel. This difference may be attributed to the heterogeneous distribution of Pu, as the local burnup within Pu-rich agglomerates is significantly higher than the pellet-average burnup of 72.8 GWd/t. Such elevated local burnup is likely to affect not only the microstructure of the Pu-rich agglomerates themselves but also that of the surrounding matrix.

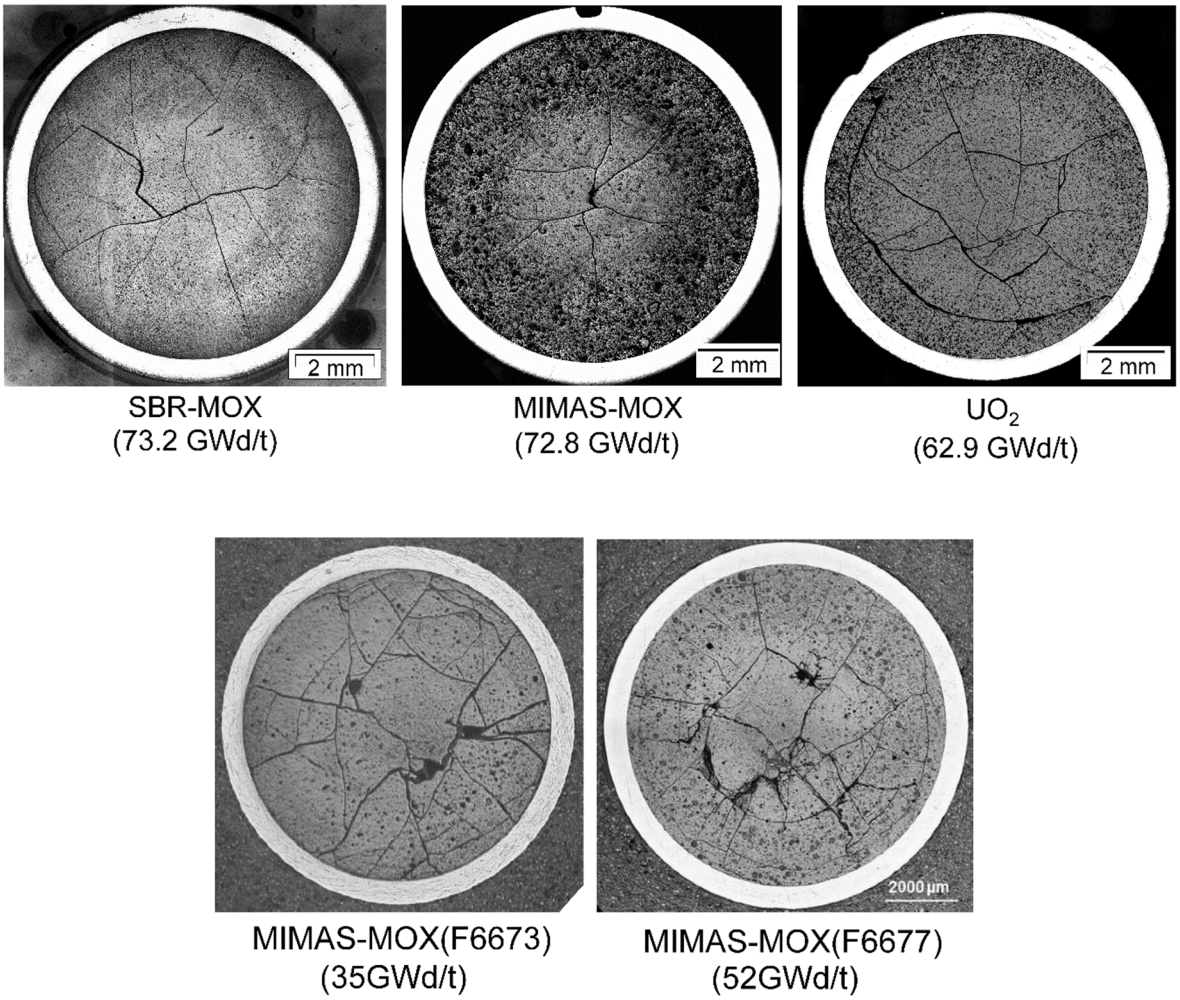


Figure 11　Ceramography on the cross-section of fuel rods after irradiation [1]

Figure 12 and Figure 13 show Pu distribution at radial positions on the cross sections of the SBR-MOX and the MIMAS-MOX fuels irradiated in the Halden reactor. The relative radial positions of 0 R and 1 R correspond to the center and periphery of the fuel pellet, respectively. The SBR-MOX fuel sample shown in Figure 12, irradiated to 64.2 GWd/t, exhibits a homogenous distribution of Pu, although several small spots with elevated Pu concentrations are observed. In contrast, the MIMAS-MOX fuel irradiated to 63.7 GWd/t shown in Figure 13 exhibits a heterogeneous Pu distribution. Pu rich agglomerates remain discernible even after irradiation up to a burnup of 63.7 GWd/t.

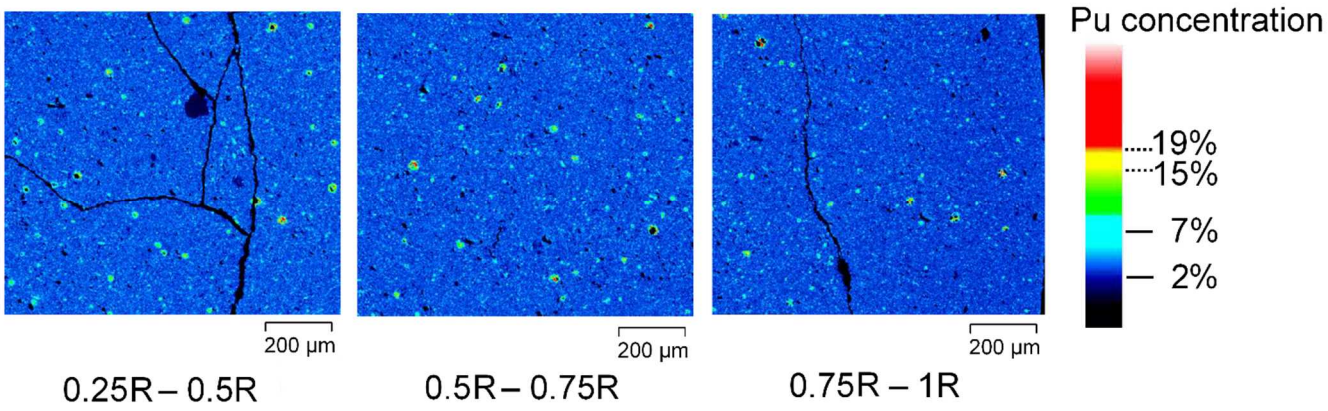


Figure 12 Pu mapping at different radial positions on the SBR-MOX fuel irradiated up to 64.2 GWd/t in the Halden reactor [1]

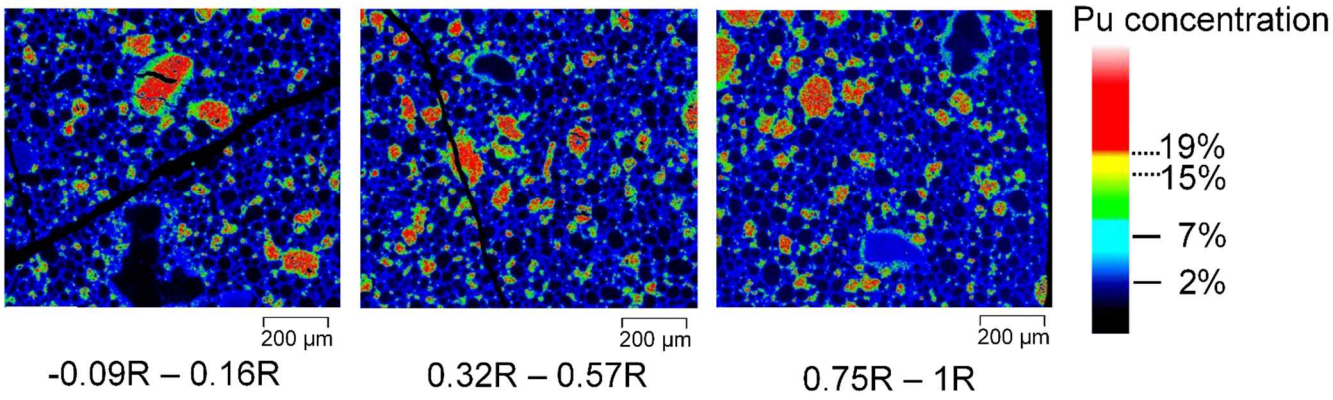


Figure 13 Pu mapping at different radial positions on the MIMAS-MOX fuel irradiated up to 63.7 GWd/t in the Halden reactor [1]

Figure 14 shows the radial Pu distribution in cross sections of the MIMAS-MOX fuels with 14.3 % Pu after irradiation at the BR2 reactor. Samples (a) and (b) were extracted from the fuel rod F6673 as listed in Table 5, while samples (c) and (d) were obtained from the fuel rod F6678, which was fabricated in the same batch as F6673 and F6677 and irradiated in the BR2 reactor together with them.

Samples (a) and (c) in Figure 14 were from a lower linear heat rate (LHR) position than the average while the samples (b) and (d) were from a higher LHR position. When the samples (b) and (c) are compared, they have almost the identical burnup value. However, Pu

concentration especially around the center is lower in the sample (b) than in the sample (c). This is considered due to diffusion of Pu activated by high temperature attributed to the higher linear heat rate. Although the diffusion of Pu is somewhat observed, all the samples (a) to (d) show a heterogeneous Pu distribution even after irradiation.

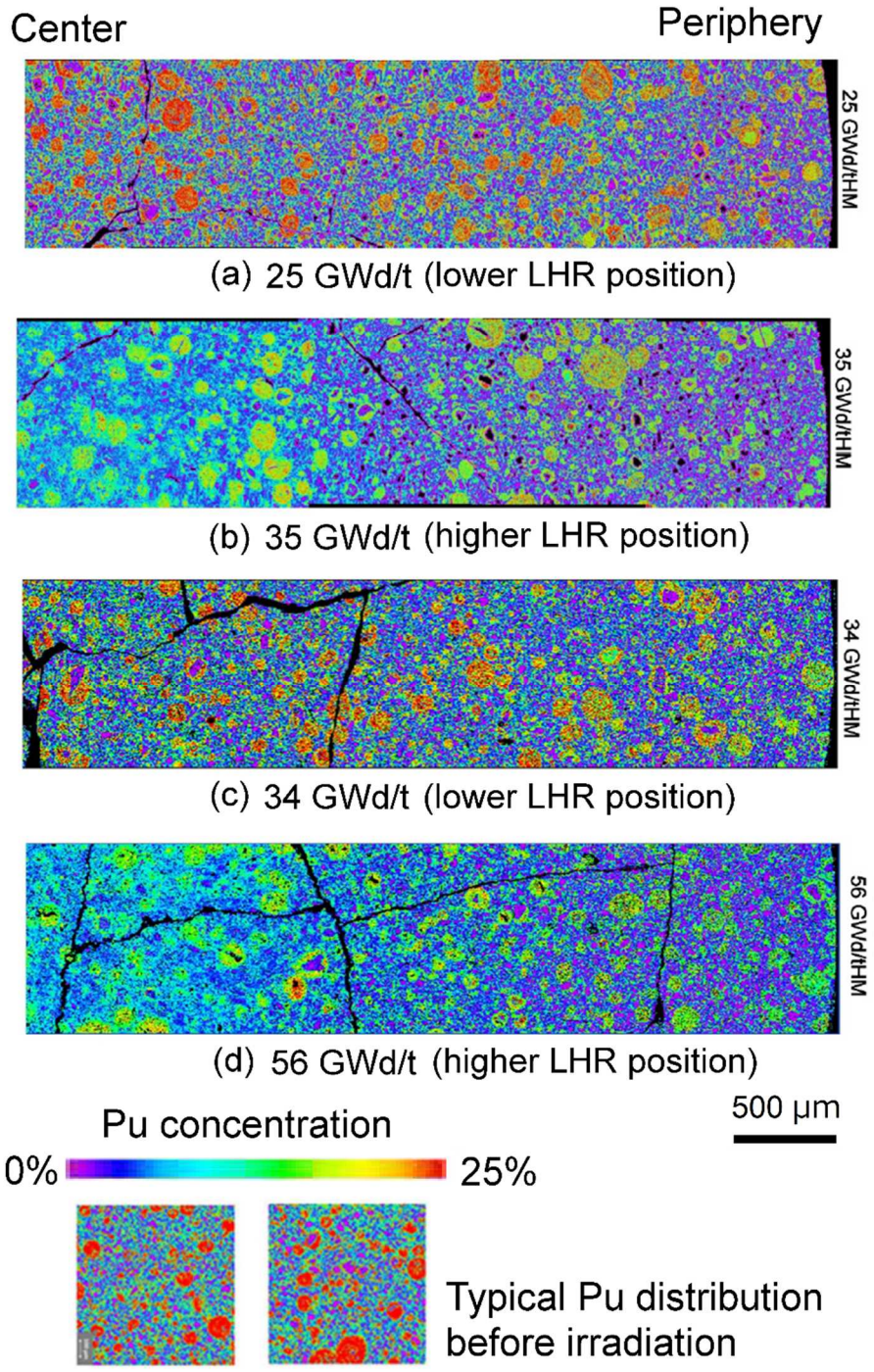


Figure 14 Pu mapping on the MIMAS-MOX fuel samples taken from different axial positions of the two fuel rods irradiated in the R2 reactor [1]

Figure 15 presents the results of line scanning for Nd along the radius on the MIMAS-MOX fuel irradiated in the Halden reactor. It shows that the amount of Nd depends on the location whether it is on U agglomerates, intermediate phase, and Pu rich agglomerates. The concentrations of Nd in terms of weight percentage were approximately 0.2%, 0.7%, and 1.3%, in U agglomerate, intermediate phase, and Pu-rich agglomerate, respectively.

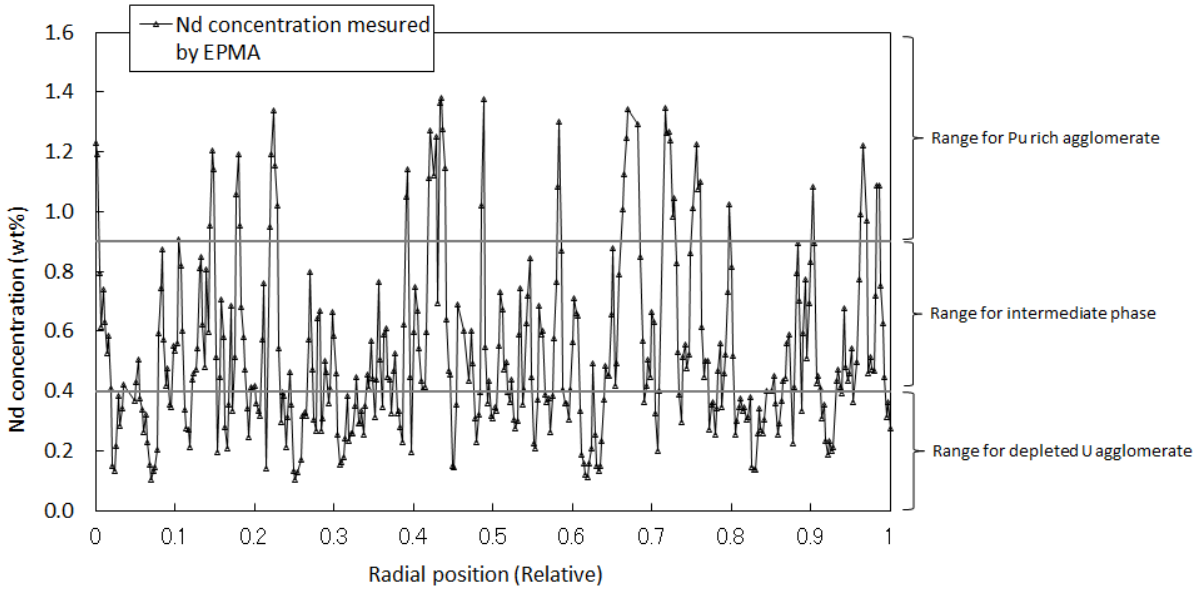


Figure 15 Nd content measured with EPMA line scanning along the radius on the MIMAS-MOX fuel irradiated up to 63.7 GWd/t in the Halden reactor [29]

Figure 16 shows distributions of fission products and plutonium across a Pu rich agglomerate which located at 3/4 radius from the center of the sample irradiated at a high LHR up to a burnup of 35 GWd/tHM. The line scanning was performed in the range of 119 μm across the Pu rich agglomerate. When we focus on the neodymium distribution, its concentrations are approximately 0.05 %, 0.2 % and 0.5 % for the U agglomerate, intermediate phase and Pu rich agglomerate.

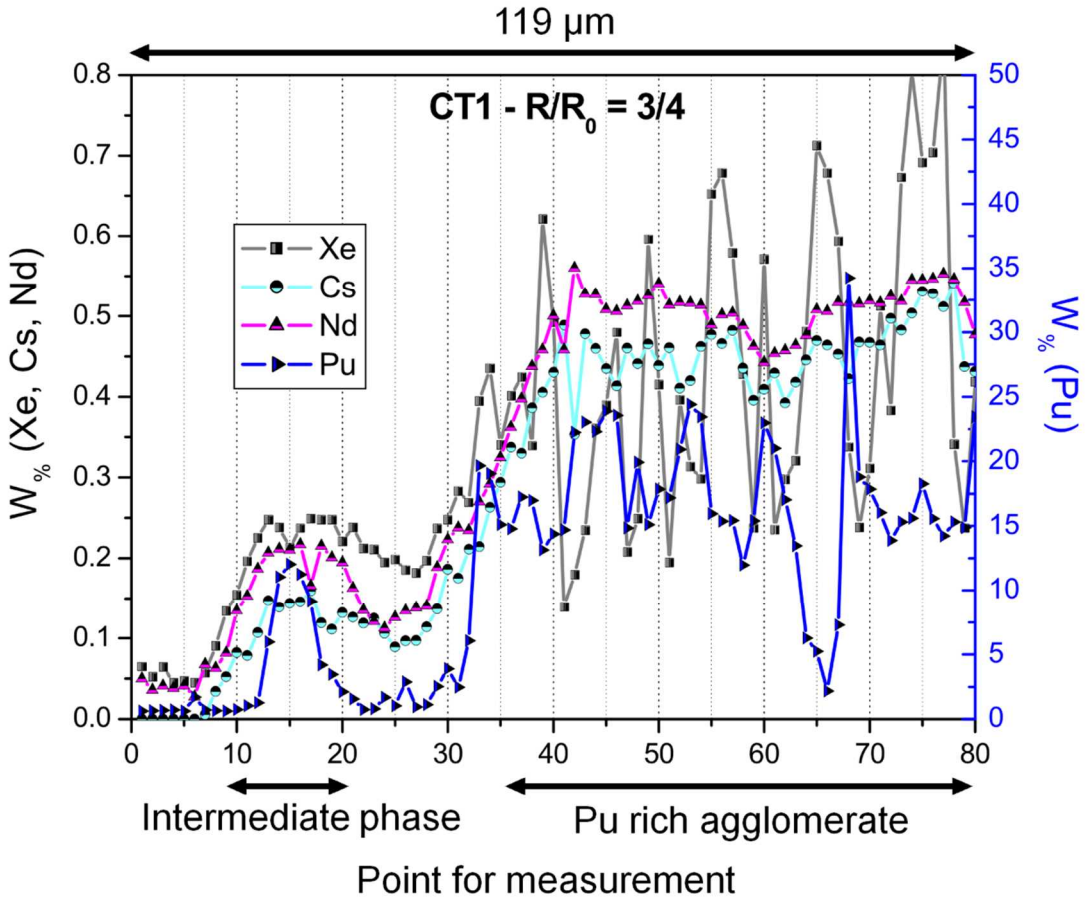


Figure 16　Elemental analysis across a Pu rich agglomerate on the sample irradiated at a high LHR up to a burnup of 35 GWd/tHM [39]

3-3-2 Results of thermal conductivity measurement

Figure 17 shows the thermal conductivity of all samples listed in Table 6. The thermal conductivity of all the samples decreases as the temperature increases. The thermal conductivity of the unirradiated fuel tends to decrease as Pu content increases. These tendencies agree with results of other previous studies [4][40]. Although the microstructures of the SBR-MOX fuel and the MIMAS-MOX fuel are different, their thermal conductivities before irradiation are similar when they have the same Pu content (8.4 %). The heterogeneous microstructure of the MIMAS-MOX fuel with Pu rich agglomerates does not seem to affect the thermal conductivity. Degradation in the thermal conductivity via irradiation is confirmed in Figure 17. Figure 18 and Figure 19 focus on thermal conductivity of the irradiated fuels in Figure 17. Note that thermal conductivity measurements for the UO_2 fuel in Figure 17 are identical with the data

[16] in Figure 3. Figure 17 is corrected for 95 % TD while Figure 3 is corrected for 100 % TD.

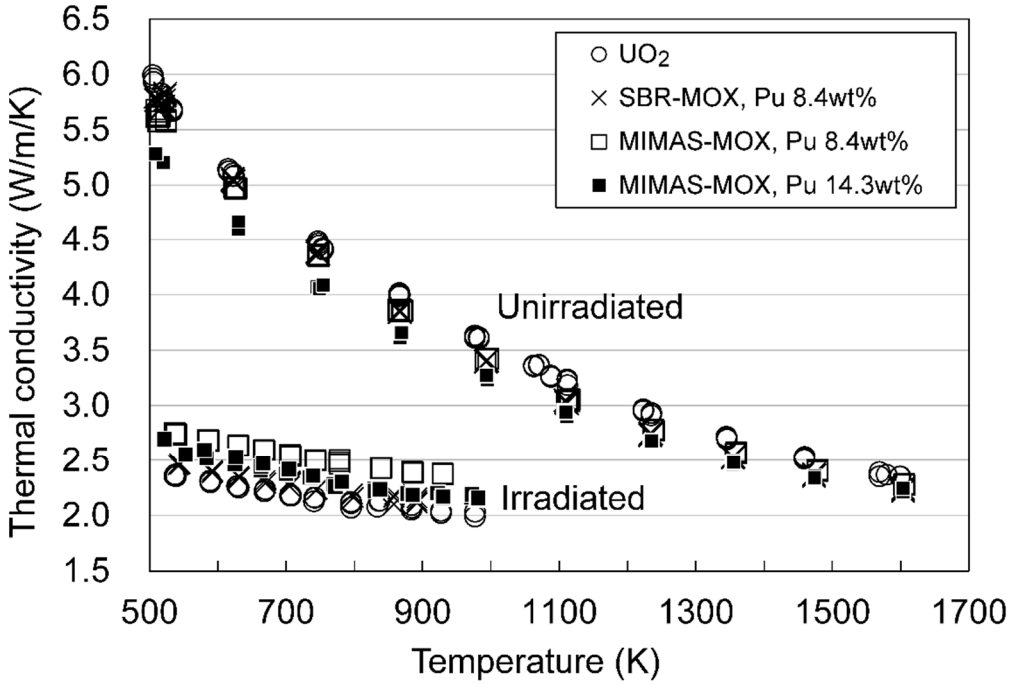


Figure 17 Thermal conductivity of unirradiated and irradiated UO_2, SBR-MOX, and MIMAS-MOX fuels with 95 % TD [16]

Figure 18 shows thermal conductivity of the UO_2 fuel, the SBR-MOX fuel and the MIMAS-MOX fuel irradiated in the Halden reactor. In Figure 18, the thermal conductivity of the MIMAS-MOX fuel sample is the highest within the temperature range of about 500 K to about 900 K. The SBR-MOX fuel sample has slightly higher thermal conductivity compared to the UO_2 fuel sample, although the thermal conductivity of the UO_2 fuel sample was the highest in the unirradiated fuel samples, as shown in Figure 17.

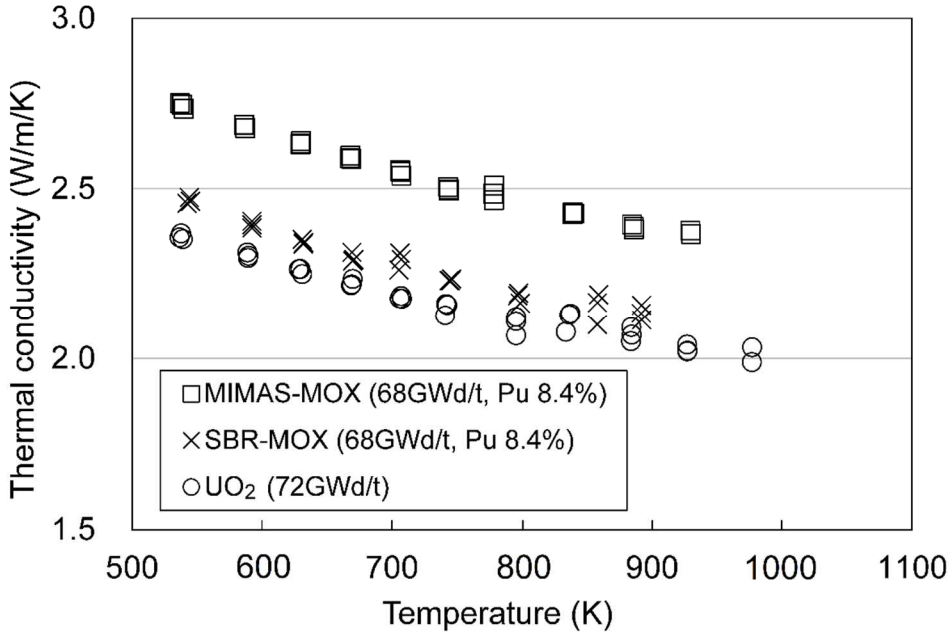


Figure 18　Thermal conductivity of UO_2, SBR-MOX, and MIMAS-MOX fuels irradiated in the Halden reactor [16]

Figure 19 shows the thermal conductivity of the MIMAS-MOX fuel samples irradiated in the Halden reactor and in the BR2 reactor. The thermal conductivity of the MIMAS-MOX fuel with a burnup of 68 GWd/t is higher than those the burnups of 34 GWd/t and 50 GWd/t. There is almost no difference in thermal conductivity between the MIMAS-MOX fuel with the burnups of 34 GWd/t and 50 GWd/t.

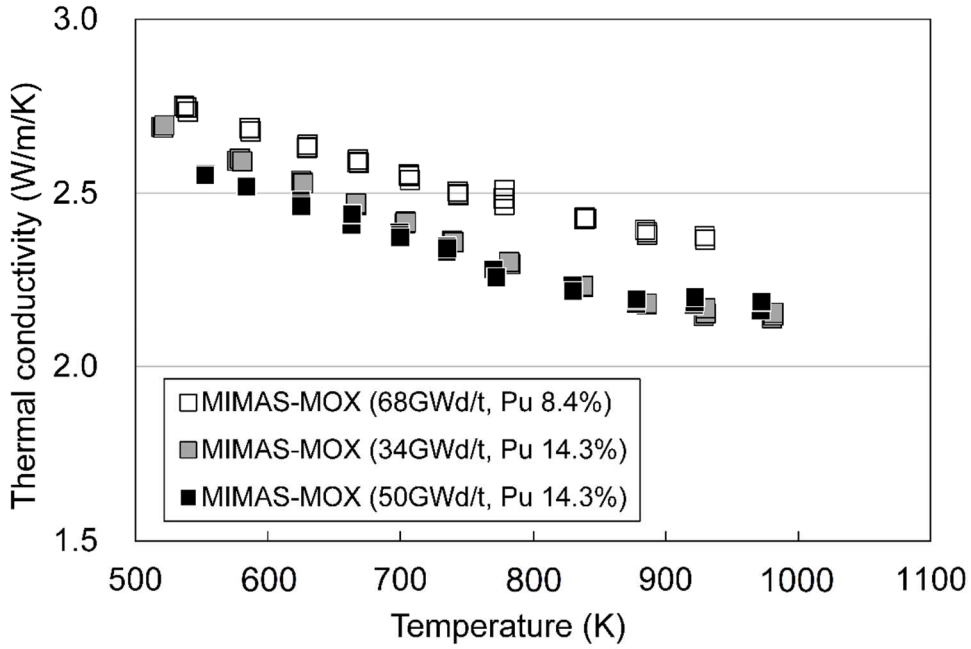


Figure 19　Thermal conductivity of MIMAS-MOX fuels irradiated in the Halden reactor and the BR2 reactor [16]

3-4 Discussion

3-4-1 Discussion on the relation between Pu distribution and burnup distribution

Table 7 and Table 8 present the ratios of Pu content to the entire average in U agglomerate, intermediate phase, and Pu-rich agglomerate. They are 0.23, 0.79, and 1.86, respectively for the unirradiated MIMAS-MOX fuel with 8.4 % Pu, and 0.18, 0.67, and 1.85 for the unirradiated MIMAS-MOX fuel with 14.3 % Pu. These ratios have been standardized with the value in the U agglomerate and are shown in Table 9.

Figure 15 presents 0.2 %, 0.7 %, and 1.3 % in average Nd content, respectively in U agglomerate, intermediate phase, and Pu-rich agglomerate for the irradiated MIMAS-MOX fuel with 8.4 % Pu while Figure 16 presents 0.05 %, 0.2 % and 0.5 % for the irradiated MIMAS-MOX fuel with 14.3 % Pu. These ratios also have been standardized with the value in U agglomerate and are shown in Table 9.

Table 9 The ratios of plutonium and neodymium contents among U agglomerate, intermediate phase and Pu-rich agglomerate.

Type of MIMAS-MOX	Analyzed element	U agglomerate	Intermediate phase	Pu-rich agglomerate
8.4 % Pu	Pu content in unirradiated state	1	3.43	8.09
	Nd content in irradiated state	1	3.5	6.5
14.3 % Pu	Pu content in unirradiated state	1	3.72	10.3
	Nd content in irradiated state	1	4.0	10.0

In theory, the distribution of a fission product of Nd is expected to be coincident with that of a fissile element of Pu. Table 9 support this expectation although there is a little discrepancy at the Pu-rich agglomerate of the MIMAS-MOX fuel with 8.4 % Pu. Since the effect of burnup on thermal conductivity is derived from fission products and lattice defects generated by fission fragments, it depends on the initial Pu content.

3-4-2 Discussion on the effect of oxygen to metal ratio on thermal conductivity

Oxygen to metal (O/M) ratio is known to give an effect on the thermal conductivity [4]. This is because the O/M ratio is an index of the number of lattice defect such as vacancy and interstitial atom which disturb the thermal flow or phonon conduction. When the unirradiated SBR-MOX and MIMAS-MOX fuel samples with a Pu content of 8.4 % are compared in Figure 17, their thermal conductivities are similar regardless of the different O/M ratios: 1.979 and 2.023 as indicated in Table 2. However, their absolute values of deviation from stoichiometry, which are 0.021 for the SBR-MOX and 0.023 for the MIMAS-MOX, are almost identical. A molecular dynamics study has confirmed that there is the almost symmetric effect of the hypo-

and hyper-stoichiometry in UO_2 on the thermal conductivity [41]. If this is applicable for the SBR-MOX and the MIMAS-MOX fuels, we can assume that the O/M ratios of 1.979 and 2.023 made a similar contribution in degradation of the thermal conductivity.

3-4-3 Discussion on the effect of plutonium on thermal conductivity

In Figure 18, the thermal conductivity of the UO_2 fuel is lower than those of the SBR-MOX fuel and MIMAS-MOX fuel. One of the reasons could be their burnups. The UO_2 fuel had a burnup of 72 GWd/t which was higher than 68 GWd/t of the SBR-MOX fuel and MIMAS-MOX fuel. However, other reasons why the thermal conductivity degradation due to irradiation is more significant in the UO_2 fuel than in the MOX fuel are pointed out in [14] as follows.

(a) Pu, which is a cause of the thermal conductivity degradation, is consumed by fission in MOX fuel, whereas Pu is produced in the UO_2 fuel via neutron absorption of U.

(b) The fission products that form a solid solution in the oxide cause the thermal conductivity degradation. Their amount is larger in the UO_2 fuel than in the MOX fuel [42][43]

(c) The diffusion coefficient of Pu atoms being higher than that of U atoms facilitates the annealing of irradiation defects causing thermal conductivity degradation [44].

In addition, the reason why the thermal conductivity of the irradiated MIMAS-MOX fuel could be higher than that of the other two fuels is considered as follows.

(d) Fission products and radiation damage, which disturb the thermal flow or phonon conduction, are localized in Pu rich agglomerates compared with those in U agglomerates. A less degradation in thermal conductivity is expected in the U agglomerate. Accordingly, the U agglomerate can play a role of fast path for thermal flow. This leads to less degradation of thermal conductivity of the MIMAS-MOX fuel compared to the SBR-MOX and UO_2 fuels that have a homogeneous distribution of the fission products and radiation damage.

In Figure 19, the thermal conductivity of the MIMAS-MOX fuel with a burnup of 68 GWd/t is higher than those the burnups of 34 GWd/t and 50 GWd/t regardless of its higher burnup. These thermal conductivities could result from the effect of Pu distribution as Figure 9 and Figure 10 shows difference in Pu distribution between the MIMAS-MOX fuels with 8.4 % Pu and 14.3 % Pu. However, it is to be noted that the thermal conductivity assessed from thermal diffusivity in this study has a relative uncertainty of 10% [11][37]. It could be due to the relative uncertainty.

In the next chapter, we discuss the effect of Pu on the thermal conductivity in MOX fuel with homogeneous Pu distribution first and then the effect of heterogeneous Pu distribution.

4. Modeling of the thermal conductivity of MOX fuel with heterogeneous Pu distribution

This chapter presents a model formula for the thermal conductivity of homogeneous MOX fuel, i.e. (U, Pu)O_2 focusing on the resistance effect of impurity such as plutonium, fission products etc., on phonon conduction. Then the effect of the heterogeneous Pu distribution is modeled based on the idea of thermal resistance circuit. The model formula is applied to the actual MIMAS-MOX fuels shown in Chapter 3. The thermal conductivity evaluated from the model formula is compared with the measurements of thermal conductivity of the MIMAS-MOX fuels. The contents of this chapter are from the publication [45] of the author.

4-1 Modeling of thermal resistivity of U-Pu mixed oxide

4-1-1 Relation of phonon scattering and thermal resistivity

The thermal conductivity k of a ceramic material can be derived by assuming phonon conduction. This is expressed by Equation (**5**), where c is the specific heat, v_s is the phonon velocity (or sound velocity), Λ is the mean free path, and τ is the relaxation time [46][47]. The relationship among the phonon velocity, the mean free path, and the relaxation time is expressed by Equation (**6**).

$$k = \frac{1}{3} c v_s \Lambda = \frac{1}{3} c v_s^2 \tau \tag{5}$$

$$\Lambda = v_s \tau \tag{6}$$

Because thermal resistivity is defined as the reciprocal of thermal conductivity, the thermal resistivity for phonon conduction denoted by ρ is expressed by Equation (7)

$$\rho = \frac{3}{c v_s \Lambda} = \frac{3}{c v_s^2 \tau} \tag{7}$$

From Equation (6), it can be observed that the reciprocal of the relaxation time corresponds to the number of phonon scatterings per unit time, denoted by N.

$$\frac{\mathbf{1}}{\boldsymbol{\tau}} = \frac{\boldsymbol{v_s}}{\boldsymbol{\Lambda}} = \boldsymbol{N} \tag{8}$$

Equation (9), derived from Equations (7) and (8), indicates that thermal resistivity is proportional to the number of phonon scatterings per unit time.

$$\boldsymbol{\rho} = \frac{\mathbf{3}}{\boldsymbol{c v_s^2}}\left(\frac{\mathbf{1}}{\boldsymbol{\tau}}\right) = \frac{\boldsymbol{3N}}{\boldsymbol{c v_s^2}} \tag{9}$$

The number of phonon scatterings per unit time depends on the type and concentration of lattice defects, which act as phonon scattering sources. The total number of phonon scatterings per unit time is expressed by Equation (10) and can be considered as the sum of the number of scatterings caused by different sources, such as impurity atoms, lattice defects, grain boundaries, and phonon-to-phonon interactions (Umklapp process), denoted by the subscripts imp, def, gb, and u, respectively.

$$\boldsymbol{N = N_{imp} + N_{def} + N_{gb} + N_u + \cdots\cdots = \frac{1}{\tau_{imp}} + \frac{1}{\tau_{def}} + \frac{1}{\tau_{gb}} + \frac{1}{\tau_u} + \cdots\cdots} \tag{10}$$

The thermal resistivity of unirradiated UO_2 is expressed by Equation (**11**), assuming that the number of all phonon scatterings per unit time in UO_2 is denoted by N_{UO2}.

$$\boldsymbol{\rho_{unirr_{UO2}} = \frac{3N_{UO2}}{c v_s^2}} \tag{11}$$

The thermal resistivity of unirradiated (U, Pu)O_2 is expressed by Equation (12), which includes the additional number of phonon scatterings per unit time caused by the presence of Pu atoms, denoted by N_{Pu}. This assumes that the specific heat and sound velocity of (U, Pu)O_2 are the same as those of UO_2 [48][49].

$$\boldsymbol{\rho_{unirr_{MOX}} = \frac{3}{c v_s^2}(N_{UO2} + N_{Pu}) = \frac{3N_{UO2}}{c v_s^2}\left(1 + \frac{N_{Pu}}{N_{UO2}}\right) = \left(1 + \frac{N_{Pu}}{N_{UO2}}\right)\rho_{unirr_{UO2}}} \tag{12}$$

The thermal resistivity of irradiated (U, Pu)O_2 is expressed by Equation (13), which incorporates the additional number of phonon scatterings per unit time caused by all the effects arising from burnup, denoted by N_{Bu}. This assumes that the effect of burnup on the specific heat

and sound velocity is negligible [50].

$$\rho_{MOX} = \frac{3}{cv_s^2}(N_{UO2} + N_{Pu} + N_{Bu})$$

$$= \frac{3N_{UO2}}{cv_s^2}\left(1 + \frac{N_{Pu}}{N_{UO2}} + \frac{N_{Bu}}{N_{UO2}}\right)$$

$$= (1 + C_{Pu} + C_{Bu})\rho_{unirrUO2} \quad (13)$$

$$where\ C_{Pu} = \frac{N_{Pu}}{N_{UO2}} \quad C_{Bu} = \frac{N_{Bu}}{N_{UO2}}$$

Equation (13) indicates that the thermal resistivity of irradiated (U, Pu)O_2 can be expressed as the thermal resistivity of unirradiated UO_2 multiplied by a correction term; this correction term is composed of the ratios of the increase in the number of phonon scatterings per unit time caused by Pu atoms and the burnup effect. The burnup effect encompasses all the effects arising from burnup, including fission products, lattice defects, and Pu atoms generated from neutron absorption by U. In the subsequent sections, we will discuss and determine the correction coefficients C_{Pu} and C_{Bu} in Equation (13).

4-1-2 Effect of Pu content on thermal resistivity

(a) Review of experimental data on the effect of Pu content

The effect of Pu content on thermal conductivity of unirradiated MOX fuel was experimentally studied by Gibby [40]. The experimental study have shown that the thermal conductivity of (U, Pu)O_2 decreases with increasing Pu content up to 30 % PuO_2. As shown in Chapter 3, we also performed thermal conductivity measurements using the laser flash method on unirradiated UO_2 fuel, homogeneous MOX fuel containing 8.4 % Pu, and heterogeneous MOX fuels containing 8.4 % and 14.3 % Pu in the weight ratio of Pu to heavy metals, which is nearly identical to the atomic ratio Pu/(U+Pu). The conductivity measurements in Chapter 3 and in [40] were converted to thermal resistivity, which is plotted in Figure 20 as a function of Pu content. The two sets of thermal resistivities are in good agreement and indicate that the

thermal resistivity of MOX fuel increases with Pu content.

Duriez et al. [4] performed thermal conductivity measurements on unirradiated homogeneous and heterogeneous MOX fuels with Pu content ranging from 3 to 15 wt% using the laser flash method. They observed that the thermal conductivity of (U, Pu)O_2 was lower than that of UO_2. However, they did not provide a quantitative relationship between the thermal conductivity and Pu content. Martin [51], Philipponneau [52], and Carbajo et al. [48] performed reviews of thermal conductivity measurements on (U, Pu)O_2. Based on their reviews, it can be concluded that the thermal conductivity of (U, Pu)O_2 is lower than that of UO_2; however, the quantitative impact of the Pu content in the range of 3–30 wt% on the thermal conductivity remains unclear. Staicu [13] attributed this unclear impact to the overlapping effect of Pu content and stoichiometry on thermal conductivity.

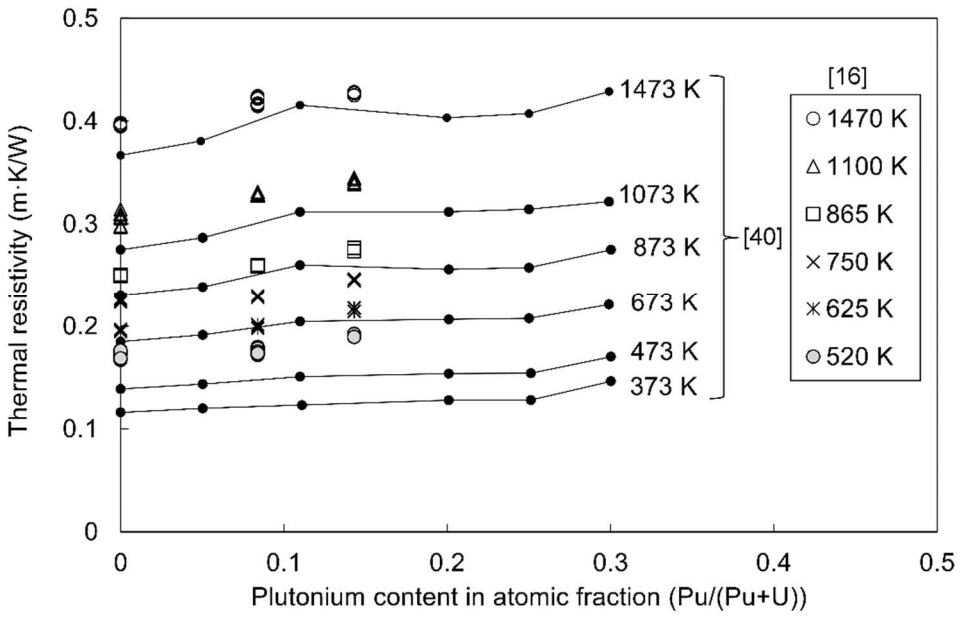


Figure 20 Thermal resistivity of MOX fuels as a function of Pu content

(b) Review of theoretical analysis of the effect of Pu content

When (U_{1-y}, Pu_y)O_2 is treated as a binary solid solution, the thermal resistivity of (U_{1-y}, Pu_y)O_2 is expected to increase parabolically with Pu content up to y = 0.5, according to the

phonon conduction models proposed by Klemens [53] and Abeles [54]. This behavior arises because Pu ions act as impurity scattering phonon in UO_2, while U ions play the same role in PuO_2. The middle composition at $y = 0.5$ provides the maximum resistivity.

Recently, the effect of Pu content on thermal conductivity has been investigated using molecular dynamics simulations [55][56][57]. Nichenko et al. developed a function of Pu content to correct the thermal conductivity of unirradiated UO_2 fuel to that of unirradiated MOX fuel, i.e., $(U_{1-y}, Pu_y)O_2$, as expressed by Equations (14) and (15) [56] using the results of the simulation and the experimental measurements reported in [40].

$$\boldsymbol{k_{\mathrm{unirr_{MOX}}} = f(y) \cdot k_{\mathrm{unirr_{UO2}}}} \tag{14}$$

$$\boldsymbol{f(y) = 1 - 0.687y + 1.0302y^2 - 0.4056y^3} \tag{15}$$

Equation (15) indicates that the thermal conductivity is minimized at $(U_{0.54}, Pu_{0.46})O_2$. The thermal conductivity given by Equation (14) can be converted into thermal resistivity, as shown in Equation (16). Equation (17) expresses $f^{-1}(y)$ that is the result of approximating the reciprocal function of Equation (17) with a cubic formula.

$$\boldsymbol{\rho_{\mathrm{unirr_{MOX}}} = f^{-1}(y) \cdot \rho_{\mathrm{unirr_{UO2}}}} \tag{16}$$

$$\boldsymbol{f^{-1}(y) = 1 + 0.7705y - 1.1243y^2 + 0.4173y^3} \tag{17}$$

Comparing Equations (13) and (16) assuming an unirradiated condition, the correction coefficient of C_{Pu} is expressed by Equation (18) as a function of Pu content.

$$\boldsymbol{C_{Pu} = 0.7705y - 1.1243y^2 + 0.4173y^3} \tag{18}$$

(c) Comparison of the correction coefficients from theoretical analysis and measurements

The thermal resistivities of the MOX fuel in Figure 20 were averaged for each Pu content and temperature. Then, the ratio of the averaged thermal resistivity of the MOX fuel to that of the UO_2 fuel was calculated. This ratio corresponds to $(1+C_{Pu})$ in Equation (13) and $f^{-1}(y)$ in Equation (16). All the evaluated ratios are plotted as a function of Pu content in Figure 21. Figure 21 shows that Equation (17) almost agrees with the ratios obtained from the measurements although variation in the ratios is relatively large. When Pu content is low, the number of phonon scatterings per unit time caused by the presence of Pu atoms is considered to linearly increase with Pu content. Accordingly, the correction coefficient of C_{Pu} has a linear dependence with the Pu content and the simple linear approximation by Equation (19) derived from fitting of the ratios obtained from the measurements is also effective in representing $f^{-1}(y)$ up to a Pu fractional content of 0.3.

$$\boldsymbol{f^{-1}(y) = 1 + C_{Pu} = 1 + 0.6y} \tag{19}$$

In this section, we conclude that the thermal resistivity of unirradiated $(U_{1-y}, Pu_y)O_2$, i.e., homogeneous MOX fuel, depends on Pu content as described by Equation (13) in conjunction with Equation (18). The simple linear model by Equation (19) shows a better agreement with the measurements up to a Pu fractional content of 0.3 as shown in Figure 21. Accordingly, Equation (19) is useful for estimation of the effect of Pu, if Pu content is up to 0.3. However, we need to discuss thermal resistivity of $(U_{1-y}, Pu_y)O_2$ with a Pu content more than 0.3. Thus, Equation (17), namely Equation (18) is used for the following discussion.

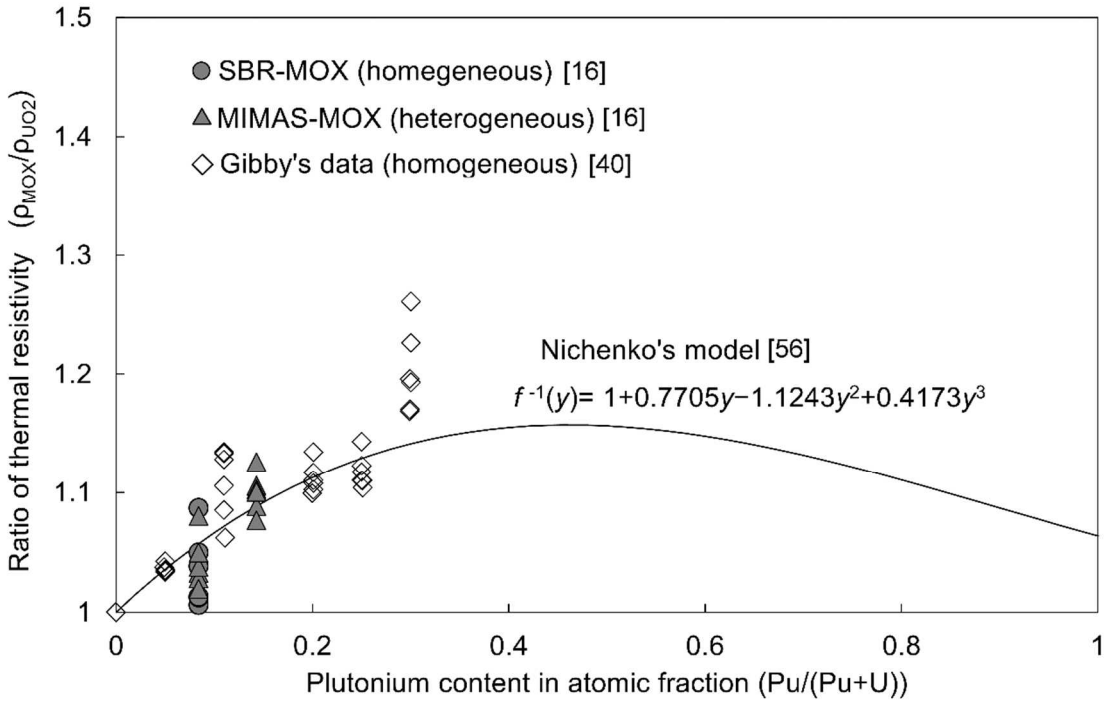


Figure 21　Ratio of the thermal resistivity of MOX fuel to that of UO2 fuel as a function of Pu content

4-1-3 Review of the effect of burnup on thermal resistivity

In irradiated MOX and UO_2 fuels, phonons are scattered by fission products, irradiation defects generated by irradiation and fission spikes, and Pu generated from neutron absorption by U, in addition to the scattering mechanisms present in unirradiated fuel. The correction coefficient C_{Bu} in Equation (13) represents the ratio of the number of additional phonon scatterings caused by burnup effects to the number of intrinsic phonon scatterings in unirradiated UO_2 fuel. A characteristic of the burnup effect is that irradiation defects can be annealed at elevated temperatures [1][6][11][58][64]. Consequently, the correction coefficient C_{Bu} is influenced by both burnup and temperature.

Ohira et al. [58] measured thermal conductivity of UO_2 fuel irradiated up to 61 GWd/t using laser flash method and they proposed a model formula for the thermal resistivity attributed to the burnup effect. This burnup-induced thermal resistivity corresponds to $C_{\mathrm{Bu}} \cdot \rho_{\mathrm{unirr_UO2}}$

in Equation (13). Lanning [26] subsequently modified the model formula to cover both UO_2 and MOX fuels, resulting in Equation (20). Table 10 presents the functions [58] constituting Equation (20), where *Bu* represents burnup in GWd/t-HM, and *T* denotes temperature in K. Please note that Equation (20) applies to fuel with 95% theoretical density.

$$\boldsymbol{C_{\mathrm{Bu}} \cdot \rho_{\mathrm{unirr_{UO2}}} = h_1(Bu) + (1 - 0.9\exp(-0.04Bu))h_2(Bu)h_3(T)} \qquad (20)$$

Table 10 Functions to model the effects of burnup on thermal resistivity and modeling functions [58]

Effect of fission products	$h_1(Bu) = 0.00187 \cdot Bu$
Effect of irradiation defects	$h_2(Bu) = 0.038 \cdot Bu^{0.28}$
Annealing effect on irradiation defects	$h_3(T) = 1/(1+396\exp(-6380/T))$

In the measurement performed by Ohira et al. [58], the thermal conductivity of irradiated UO_2 fuel was measured using the laser flash method during both a temperature-ascent process from 700 K to 1700 K and a subsequent temperature-descent process from 1700 K to 700 K. They hypothesized that the measurements obtained during the initial temperature-ascent process represented the thermal conductivity degraded by both fission products and irradiation defects. In addition, they assumed that the measurements obtained during the temperature-descent process, following the temperature-ascent process, reflected thermal conductivity degraded solely by fission products because the irradiation defects were assumed to have been annealed at elevated temperature during the initial temperature-ascent process. As a result, they developed the function $h_1(Bu)$ in Table 10 based on the measurements obtained during the temperature-descent process. Subsequently, they formulated the functions $h_2(Bu)$ and $h_3(T)$ based on the discrepancy between the measurements obtained during the temperature-ascent and temperature-descent processes.

As shown in Figure 6 in Chapter 3, we investigated the effect of burnup on the thermal conductivity of irradiated MOX fuel using the laser flash method and observed the annealing

effect. However, the irradiated MOX fuel samples fractured at approximately 930 K owing to thermal shock from laser flash. Therefore, we could not quantitatively separate the three effects shown in Table 10 because the temperature of 930 K was not high enough for annealing of irradiation defects. Therefore, we adopt Equation (20) for the thermal resistivity arising from the burnup effect, which corresponds to $C_{\mathrm{Bu}} \cdot \rho_{\mathrm{unirr_UO2}}$ in Equation (13).

4-1-4 Correction for Pu content

Ohira et al. [58] did not explicitly discuss the influence of Pu generated from neutron absorption by U on thermal conductivity. However, we assume that the effect of the generated Pu is incorporated in the effect of fission products, h_1(Bu) in Table 10 because it is assumed that the effect of generated Pu is not annealed by heating. In contrast to the generated Pu, the initial Pu content y in Equation (18) decreases with burnup; this reduction in the initial Pu content needs to be considered in Equation (18). The burnup of the initial Pu can be expressed by the fraction of fission per initial metal atom (FIMA) as well as the unit GWd/t-HM. The FIMA unit is directly comparable to the Pu atomic fraction denoted by y in Equation (18). The relationship between the two units is that 937.5 GWd/t-HM is equivalent to 1 FIMA. Taking these relationships into account, Equation (18) is modified to Equation (21).

$$\boldsymbol{C_{\mathrm{Pu}} = 0.7705\left(y - \frac{Bu}{937.5}\right) - 1.1243\left(y - \frac{Bu}{937.5}\right)^2 + 0.4173\left(y - \frac{Bu}{937.5}\right)^3} \quad (21)$$

$$\boldsymbol{y - \frac{Bu}{937.5} \geq 0}$$

4-1-5 Thermal resistivity of homogeneous MOX fuel

Figure 4 in Chapter 3 shows the thermal resistivity of unirradiated UO_2 fuel as a function of temperature as Equation (3). It can be applied to $\rho_{\mathrm{unirr_UO2}}$ in Equation (13). It is important to note that Equation (3) corrected to UO_2 fuel with 95% theoretical density. All subsequent thermal resistivity and conductivity in this discussion pertain to fuel with 95% theoretical density.

Finally, we have determined the thermal resistivity of unirradiated UO_2 fuel and all the correction coefficients in Equation (13) for calculating the thermal resistivity of unirradiated and irradiated homogeneous MOX fuel as functions of Pu content, temperature, and burnup. Figure 22 compares thermal conductivity measurements corrected to 95% theoretical density [11][16] with predictions derived from the thermal resistivity calculated using Equations (13) with (3), (20), and (21) for UO_2 and SBR–MOX fuels, which are homogeneous MOX fuels. The bold line in Figure 22 represents the measurements obtained during the temperature-ascent process from 600 K to 1400 K following the process reaching 1000 K [11]. The predictions obtained from Equations (13) with (3), (20), and (21) agree well with the measurements reported in [16]. However, the predictions overestimate the measurements for the SBR–MOX fuel irradiated up to 43 GWd/t-HM reported in [11]. The relative uncertainty of thermal conductivity measurements using the laser flash method is estimated to be 10% [11][37]. Considering this relative uncertainty, the prediction for the SBR–MOX fuel irradiated up to 43 GWd/t-HM almost falls into the range of measurement uncertainty. Consequently, we conclude that Equation (13), in conjunction with Equations (3), (**20**), and (21) is applicable for determining the thermal resistivity of UO_2 and SBR–MOX fuels, i.e., homogeneous MOX fuel.

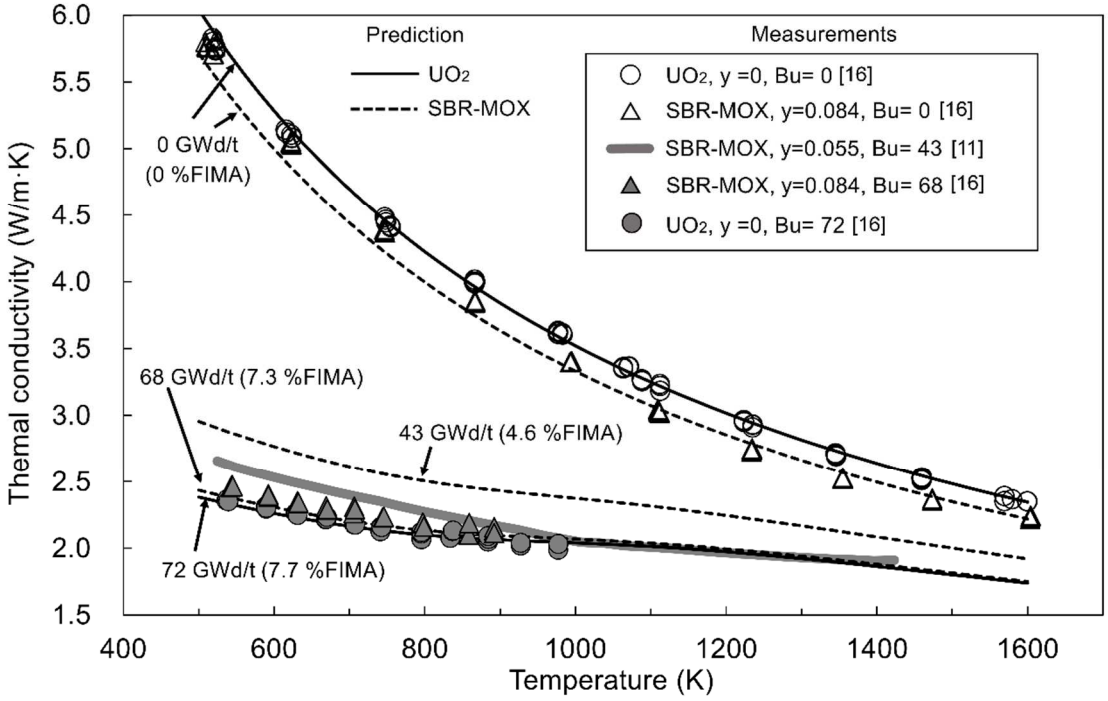


Figure 22 Comparison of prediction with measurements on thermal conductivity of MOX fuel with homogeneous Pu distribution

4-2 Modeling of thermal resistivity and conductivity of heterogeneous MOX fuel

4-2-1 Model to combine thermal resistivities connected in series and parallel

Eucken [59] investigated the thermal conductance of two mixed phases, and Loeb [60] studied the thermal conductivity of porous materials. Based on their findings, Kämpf et al. [61] and Schulz [62] developed model formulas to correct for the effect of pores in thermal conductivity measurements such as Equations (2) and (4). Their assumption was that the fuel consisted of two phases: the matrix and pores. Based on the work of Schulz [62], Kosaka et al. [12] developed a formula for the thermal conductivity of MIMAS–MOX fuel as a function of the volume fractions of the two phases, namely, the Pu-rich agglomerate and the matrix. Using the formula, they explained that the matrix of the MIMAS–MOX fuel, which had a lower burnup than average burnup, could act as a fast pathway for phonon conduction and contributed to the higher thermal conductivity of the irradiated MIMAS-MOX fuel than that of the irradiated SBR–MOX fuel. Staicu et al. [13] introduced a formula for three phases comprising

a Pu-rich agglomerate, an intermediate phase, and a U agglomerate. They also used volume fractions of the Pu-rich agglomerate, intermediate phase, and U agglomerate to formulate the heterogeneous character on thermal conductivity. However, volume fraction alone cannot capture the state of dispersion of the Pu-rich agglomerate; it cannot distinguish between the states where large agglomerates are distributed coarsely, or small agglomerates are distributed finely.

The original idea of Loeb [60] is that thermal conductance and resistance can be expressed similarly to electrical conductance and resistance. Recently, Lee [63] applied the concept of electrical resistance circuits to the study of thermal resistivity of the microcell fuel consisting of UO_2 crystal grains and molybdenum grain boundary that have different thermal resistivities. Figure 23 illustrates two examples of a simple resistance circuit. Both circuits consist of four identical resistors. One circuit exhibits an even configuration of the resistors, whereas the other exhibits an uneven configuration. As shown in Figure 23, the combined resistance is lower in the uneven configuration than in the even configuration. This result arises from combining the resistances connected in series (process (a)), followed by combining those connected in parallel (process (b)). Figure 23 demonstrates that the thermal resistivity of MIMAS–MOX fuel with heterogeneous Pu distribution can be lower than that of SBR–MOX fuel with homogeneous Pu distribution, if their total Pu contents are identical. We try to apply this concept to the thermal resistivity of MIMAS–MOX fuel.

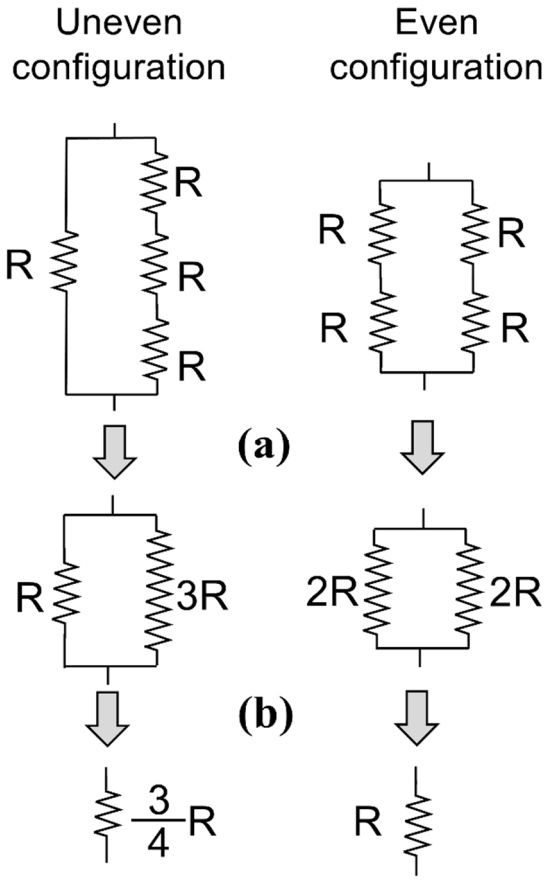


Figure 23 Comparison of combined resistances in uneven and even configurations

When thermal resistance is analogous to electrical resistance, the combined thermal resistance of thermal resistances connected in series, as illustrated in Section I of Figure 24(A), is represented by the sum of the individual thermal resistances, as described by Equation (22), assuming uniaxial thermal flow as shown in Figure 24. It is noted that thermal resistance is defined as being proportional to both thermal resistivity and length, and inversely proportional to the cross-sectional area, as indicated in Equation (22). This combining process corresponds to process (a) in Figure 23. In Equation (22), the symbols have the following meanings: R represents thermal resistance, ρ represents thermal resistivity, l represents length, and S represents cross-sectional area. The reader is referred to for the subscripts used in the symbols.

$$\boldsymbol{R_{\mathrm{I}} = R_{\mathrm{I},1} + R_{\mathrm{I},2} + R_{\mathrm{I},3} + R_{\mathrm{I},4} = \frac{1}{S_{\mathrm{I}}}\left(l_{\mathrm{I},1} \cdot \rho_{\mathrm{I},1} + l_{\mathrm{I},2} \cdot \rho_{\mathrm{I},2} + l_{\mathrm{I},3} \cdot \rho_{\mathrm{I},3} + l_{\mathrm{I},4} \cdot \rho_{\mathrm{I},4}\right)} \quad (22)$$

The average of the thermal resistivities denoted by $\bar{\rho}$, considering the length of each element, is expressed by Equation (23), where l_{tot} is the total length.

$$\bar{\rho}_{\mathrm{I}} = \frac{1}{l_{\mathrm{tot}}}\left(l_{\mathrm{I},1}\cdot\rho_{\mathrm{I},1} + l_{\mathrm{I},2}\cdot\rho_{\mathrm{I},2} + l_{\mathrm{I},3}\cdot\rho_{\mathrm{I},3} + l_{\mathrm{I},4}\cdot\rho_{\mathrm{I},4}\right) = \sum_{i,j}\left(\frac{l_{i,j}}{l_{\mathrm{tot}}}\cdot\rho_{i,j}\right) \tag{23}$$

$$where\ \ i = \mathrm{I}, \mathrm{II}, \mathrm{III}\cdots,\ \ j = 1, 2, 3\cdots$$

Equation (23) is generalized to Equation (24), considering volume denoted by v instead of length.

$$\bar{\rho}_{\iota} = \sum_{i,j}\left(\frac{v_{i,j}}{v_{i,\mathrm{tot}}}\cdot\rho_{i,j}\right) \tag{24}$$

When thermal resistances are connected in parallel to the direction of thermal flow, as illustrated in Figure 24(B), the reciprocal of the combined thermal resistance, which corresponds to the thermal conductance denoted by K, is expressed by the sum of the reciprocals of the individual sectional thermal resistances, as described by Equation (25). This combining process corresponds to process (b) in Figure 23.

$$K = \frac{1}{R} = \frac{1}{R_{\mathrm{I}}} + \frac{1}{R_{\mathrm{II}}} + \frac{1}{R_{\mathrm{III}}} + \frac{1}{R_{\mathrm{IV}}} = \frac{1}{l_{\mathrm{tot}}}\left(\frac{S_{\mathrm{I}}}{\bar{\rho}_{\mathrm{I}}} + \frac{S_{\mathrm{II}}}{\bar{\rho}_{\mathrm{II}}} + \frac{S_{\mathrm{III}}}{\bar{\rho}_{\mathrm{III}}} + \frac{S_{\mathrm{IV}}}{\bar{\rho}_{\mathrm{IV}}}\right) \tag{25}$$

The effective thermal conductivity of k_{eff} is defined as the thermal conductivity representing the state of Figure 24(C). It is noted that the thermal conductance is defined as being proportional to both effective thermal conductivity and cross-sectional area, and inversely proportional to the length as expressed Figure 24(C).

$$k_{\mathrm{eff}} = \frac{l_{\mathrm{tot}}}{S_{\mathrm{tot}}}K = \frac{1}{S_{\mathrm{tot}}}\left(\frac{S_{\mathrm{I}}}{\bar{\rho}_{\mathrm{I}}} + \frac{S_{\mathrm{II}}}{\bar{\rho}_{\mathrm{II}}} + \frac{S_{\mathrm{III}}}{\bar{\rho}_{\mathrm{III}}} + \frac{S_{\mathrm{IV}}}{\bar{\rho}_{\mathrm{IV}}}\right) = \sum_{i}\left(\frac{S_i}{S_{\mathrm{tot}}}\cdot\frac{1}{\bar{\rho}_i}\right) \tag{26}$$

In a cylindrical fuel pellet, we consider thermal flow only in the radial direction because it can be reasonably assumed that temperature gradients in the axial and hoop directions are negligible from a macroscopic perspective. Consequently, we limit our discussion of the effective thermal conductivity of heterogeneous MOX fuel using Equations (22) – (26) to the radial direction of the cylindrical fuel pellet.

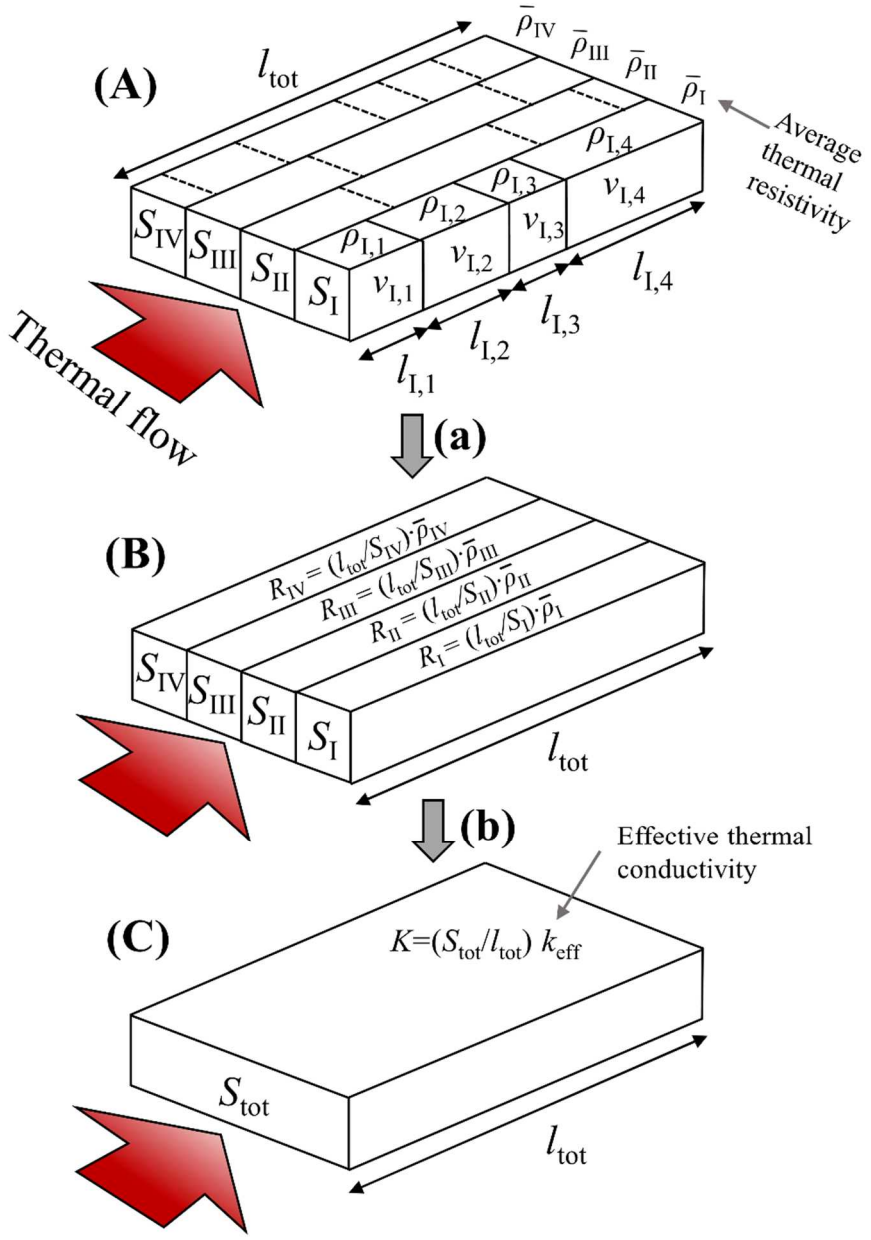


Figure 24 Schematic drawing of thermal resistances connected in series and parallel

4-2-2 Application to the heterogeneous MOX fuel

The thermal resistivity of homogeneous MOX fuel was represented by Equation (13). Substituting Equation (13) into Equation (24) yields Equation (27), which represents the weighted-average thermal resistivity of different thermal resistivities connected in series considering volume.

$$\overline{\boldsymbol{\rho}}_{\mathbf{MOX}i} = \sum_{i,j}\left(\frac{\boldsymbol{v}_{i,j}}{\boldsymbol{v}_{i,\mathbf{tot}}}\cdot \boldsymbol{\rho}_{\mathbf{MOX}_{i,j}}\right) = \sum_{i,j}\left(\frac{\boldsymbol{v}_{i,j}}{\boldsymbol{v}_{i,\mathbf{tot}}}\cdot\left(\mathbf{1}+\boldsymbol{C}_{\mathbf{Pu}_{i,j}}+\boldsymbol{C}_{\mathbf{Bu}_{i,j}}\right)\cdot \boldsymbol{\rho}_{\mathbf{unirr}_{\mathbf{UO2}}}\right) \tag{27}$$

By combining Equations (26) and (27), we obtain Equation (28), which expresses the effective thermal conductivity, k_{MOX} that is representing the thermal conductivity of the entire heterogeneous MOX fuel.

$$\begin{aligned}\boldsymbol{k}_{\mathbf{MOX}} &= \sum_{i}\left(\frac{\boldsymbol{S}_i}{\boldsymbol{S}_{\mathbf{tot}}}\cdot\frac{\mathbf{1}}{\overline{\boldsymbol{\rho}}_{\mathbf{MOX}_i}}\right)\\ &= \sum_{i}\left(\frac{\boldsymbol{S}_i}{\boldsymbol{S}_{tot}}\cdot\frac{\mathbf{1}}{\left[\sum_{i,j}\left(\frac{\boldsymbol{v}_{i,j}}{\boldsymbol{v}_{i,\mathbf{tot}}}\cdot\left(\mathbf{1}+\boldsymbol{C}_{\mathbf{Pu}_{i,j}}+\boldsymbol{C}_{\mathbf{Bu}_{i,j}}\right)\cdot\boldsymbol{\rho}_{\mathbf{unirr}_{\mathbf{UO2}}}\right)\right]}\right)\end{aligned} \tag{28}$$

4-3 Evaluation of the thermal conductivity of heterogeneous MOX fuels

4-3-1 Analysis of thermal resistivity and conductivity using Pu mapping

To determine the correction coefficients C_{Pu} and C_{Bu} using Equations (21) and (20), respectively, values of the local Pu content y and local burnup Bu are required. The local Pu content can be measured using electron probe micro analyzer (EPMA). In Chapter 3, the distribution of Pu in two types of unirradiated MIMAS–MOX fuel with 8.4 % Pu and 14.3 % Pu was observed via EPMA. Figure 25 shows the ternary Pu concentration map identical with Figure 9. In Figure 25, there are lines for sectioning. In this study, we use the ternary Pu concentration maps (such as the one shown in Figure 25) to evaluate $C_{Pu}{}_{i,j}$, $C_{Bu}{}_{i,j}$, $v_{i,j}$, $v_{i,tot}$, S_i, and S_{tot} in Equation (28) instead of full concentration maps in order to simplify the assessment.

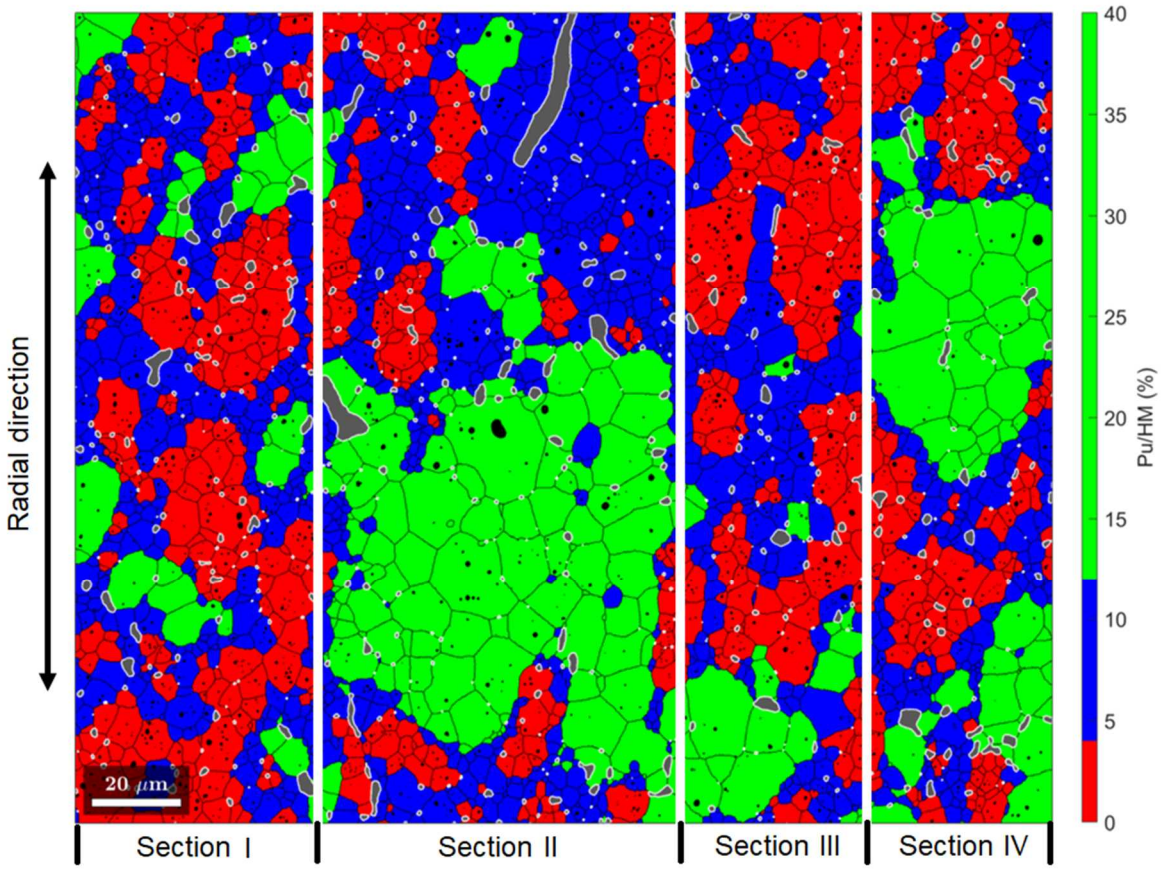


Figure 25 Ternary Pu concentration map divided into four sections for evaluation of thermal resistivity of MIMAS-MOX fuel with 8.4 % Pu

The sectioning of the map is a crucial step in evaluating the effective thermal conductivity using Equation (28). To accurately capture the impact of heterogeneous Pu distribution on the effective thermal conductivity, the sectioning should be performed in a manner that maximizes the difference in Pu content (and hence thermal resistance) among the sections, as illustrated by the white lines in Figure 25. Moreover, the sectioning should be performed along the radial direction because the thermal flow considered is solely in the radial direction of a cylindrical fuel pellet, under the assumption that thermal flows in the hoop and axial directions are negligible. Figure 25 shows the ternary Pu concentration map divided into four sections. Using finer sectioning would yield a more accurate result. However, if the Pu distributions in the neighboring sections are comparable, the level of sectioning refinement has no significant effect on the result. We think that dividing the area into four sections, as shown

in Figure 25, sufficiently captures the Pu distributions characterizing the effective thermal conductivity for the observed location in this study.

As an initial step in evaluating the effective thermal conductivity, the three average Pu contents of the three phases were converted to thermal resistivities using Equations (13) with (3), (20), and (21), with Bu = 0 for unirradiated MIMAS–MOX fuel. Table 11 presents the average Pu contents of the three phases and entire average listed in Table 7 in Chapter 3 as well as evaluated thermal resistivities at 1000 K, that is a representative temperature of fuel during normal operation, for the three phases shown in Figure 25. The thermal resistivities in Table 11 correspond to $\rho_{\mathrm{MOX}i,j}$ in Equation (27) for the unirradiated case.

Table 11 Average Pu contents and thermal resistivity of the three phases at 1000 K in the unirradiated MIMAS–MOX fuel shown in Table 7

Phase	Initial Pu content, (y)	Thermal resistivity, ($\rho_{\mathrm{MOX}i,j}$) [m·K/W]
Pu-rich agglomerate	0.177	0.313
Intermediate phase	0.075	0.299
U agglomerate	0.022	0.289
Entire average evaluated from image analysis	0.095	–

Since the local burnup depends on the local Pu content as shown with Table 9, the local burnup in irradiated MIMAS-MOX fuel is expressed by Equation (29) where y_{nom} is the nominal Pu content or the average Pu content in the observed local area in unirradiated state and Bu_{avg} is the pellet average burnup.

$$Bu = \frac{y}{y_{\mathrm{nom}}} Bu_{\mathrm{avg}} \tag{29}$$

Using Equation (29), the three Pu contents listed in Table 11 were converted to the three local burnups, assuming a specified pellet-average burnup. In this study, the entire average of 0.095 in Table 11 was used as the value of y_{nom} instead of the nominal Pu content of 0.084. The residual

initial Pu content was also evaluated using the relationship between the burnup units of FIMA and GWd/t-HM. Table 12 presents the three local burnups, the residual initial Pu contents, and the thermal resistivities calculated using Equations (13) with (3), (20), and (21), assuming a pellet-average burnup of 68 GWd/t-HM and a temperature of 1000 K. The thermal resistivities in Table 12 correspond to $\rho_{\mathrm{MOX}i,j}$ in Equation (27) for the irradiated case.

Table 12 Burnup, residual initial Pu content, and thermal resistivity of the three phases in MIMAS–MOX fuel shown in Table 11, assuming irradiation up to 68 GWd/t-HM and a temperature of 1000 K

Phase	Local burnup, (Bu) [GWd/t-HM]	Residual initial Pu content	Thermal resistivity, ($\rho_{\mathrm{MOX}i,j}$) [m·K/W]
Pu-rich agglomerate	127	0.041	0.618
Intermediate phase	54	0.017	0.451
U agglomerate	16	0.005	0.340

Subsequently, the area fractions of the three phases in each section of Figure 25 were determined through image analysis. Additionally, the width of each section was measured. Assuming that the area fraction is equivalent to the volume fraction and the width fraction is equivalent to the cross-sectional area fraction, the volume fractions of the three phases and the cross-sectional area fractions of the four sections in Figure 25 were evaluated, as presented in Table 13 and Table 14, respectively (even in Table 15 for convenience). The volume fractions in Table 13 correspond to $v_{i,j}/v_{i,\mathrm{tot}}$ in Equation (27). The cross-sectional area fractions in Tables 5 and 6 correspond to S_i/S_{tot} in Equation (28).

The average thermal resistivity $\bar{\rho}_{\mathrm{MOX}i}$ in each section in the unirradiated state was calculated by substituting the thermal resistivities $\rho_{\mathrm{MOX}i,j}$ from Table 11 and the volume fractions $v_{i,j}/v_{i,\mathrm{tot}}$ from Table 13 into Equation (27). The average thermal resistivity of each section is presented in Table 14. Finally, the effective thermal conductivity was calculated by substituting the average thermal conductivities $\bar{\rho}_{\mathrm{MOX}i}$ and the cross-sectional area fractions S_i/S_{tot} in Table

14 into Equation (28). The value of the effective thermal conductivity is also included in Table 14. The same procedure was applied to the irradiated case, using the thermal resistivities from Table 12, the volume fractions from Table 13 and cross-sectional area fractions in Table 15. The result is shown in Table 15. It should be noted that this study assumes the Pu distribution remains unchanged from its initial state throughout irradiation. Accordingly, Figure 25 which shows the unirradiated condition, was utilized for the assessment of the irradiated case.

Table 13 Volume fractions of the sections measured via image analysis on Figure 25

	Section I	Section II	Section III	Section IV
Pu-rich agglomerate ($v_{i,j}/v_{i,\mathrm{tot}}$)	0.143	0.437	0.144	0.421
Intermediate phase ($v_{i,j}/v_{i,\mathrm{tot}}$)	0.421	0.396	0.397	0.289
U agglomerate ($v_{i,j}/v_{i,\mathrm{tot}}$)	0.436	0.167	0.459	0.289

Table 14 Result of the evaluation on average thermal resistivity of the sections shown in Figure 25 and effective thermal conductivity in the unirradiated state at a temperature of 1000 K

	Section I	Section II	Section III	Section IV
Average thermal resistivity ($\bar{\rho}_{\mathrm{MOX}_i}$) [m·K/W]	0.297	0.303	0.296	0.302
Cross-sectional area fraction (S_j/S_{tot})	0.249	0.374	0.189	0.189
Effective thermal conductivity (k_{MOX}) [W/m·K]	3.34			

Table 15 Result of the evaluation on thermal resistivity and conductivity of the sections shown in Figure 25 and effective thermal conductivity assuming a burnup of 68 GWd/t-HM

	Section I	Section II	Section III	Section IV
Average thermal resistivity ($\bar{\rho}_{\mathrm{MOX}_i}$) [m·K/W]	0.426	0.505	0.424	0.489
Cross-sectional area fraction (S_j/S_{tot})	0.249	0.374	0.189	0.189
Effective thermal conductivity (k_{MOX}) [W/m·K]	2.16			

This analysis process was applied to the three additional ternary Pu concentration maps that were the same as those used for the image analysis in Chapter 3. (The results of the image analysis are shown in Table 7 of Chapter 3.) Accordingly, four maps covering a total area of approximately 150,000 μm^2 were subjected to the analysis for effective thermal conductivity. Table 16 summarizes the four effective thermal conductivities from the analysis and their simple average, where a temperature of 1000 K and burnups of 0 and 68 GWd/t-HM were assumed. We also applied the same process to the MIMAS–MOX fuel with 14.3 % Pu. Figure 26 shows the ternary Pu concentration map for the MIMAS–MOX fuel with 14.3 wt% Pu, that is identical with Figure 10. Table 16 includes the evaluated effective thermal conductivities and their simple average for the MIMAS–MOX fuel with 14.3 % Pu as well. In addition, the thermal conductivities of SBR-MOX fuel evaluated by Equation (13) in conjunction with Equations (3), (20), and (21) are listed in Table 16 for comparison.

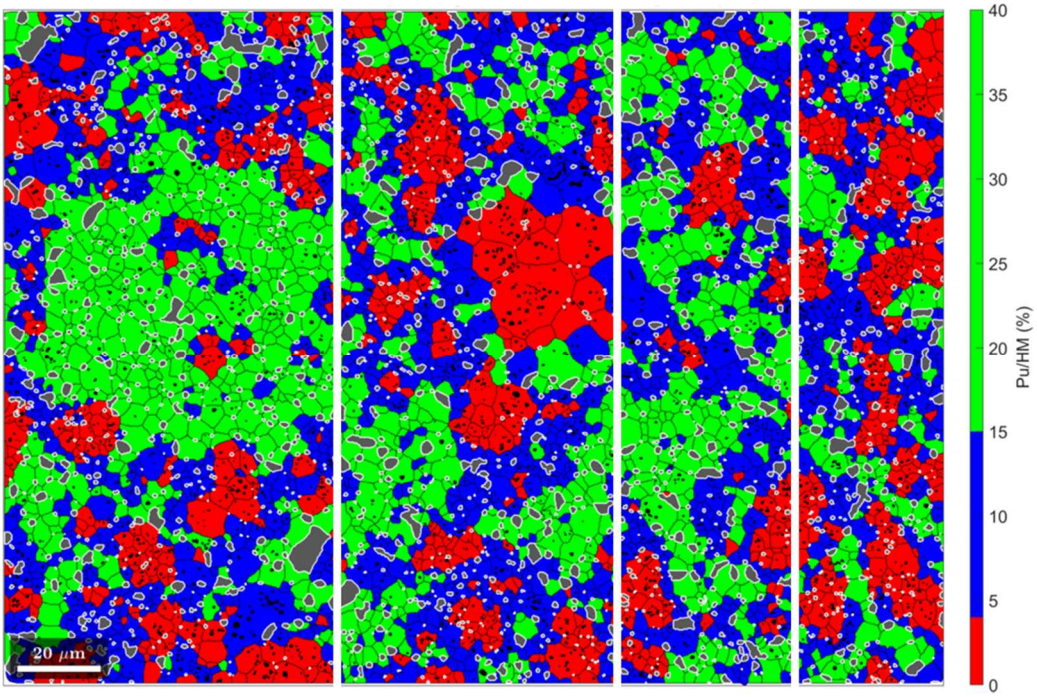


Figure 26 Ternary Pu concentration map divided into four sections for evaluation of thermal resistivity of MIMAS-MOX fuel with 14.3 % Pu

Table 16 Effective thermal conductivities evaluated from four ternary Pu concentration maps for the two kinds of MIMAS–MOX fuels and the evaluated thermal conductivity of SBR–MOX fuel at a temperature of 1000 K

Burnup [GWd/t-HM]	Nominal Pu content [wt%]	MIMAS–MOX [W/m·K]					SBR–MOX [W/m·K]
		Map 1	Map 2	Map 3	Map 4	Average	
0	8.4	3.34	3.32	3.34	3.31	3.33	3.33
	14.3	3.28	3.26	3.31	3.26	3.28	3.23
68	8.4	2.16	2.22	2.27	2.20	2.24	2.07
	14.3	2.08	2.00	2.20	2.01	2.07	2.02

In the unirradiated condition at 0 GWd/t-HM, the effective thermal conductivities of the MIMAS–MOX fuels are similar to those of the SBR–MOX fuels. As seen in Table 11, the difference in thermal resistivity among the three phases is not significant in the unirradiated condition. Therefore, a certain random distribution of the three phases makes its effective

thermal conductivity close to that of SBR–MOX fuel with homogenous Pu distribution.

In the irradiated condition at 68 GWd/t-HM, the effective thermal conductivities of the MIMAS–MOX fuel with 8.4 % Pu are higher than that of the SBR–MOX fuel with 8.4 % Pu, while the effective thermal conductivities of the MIMAS–MOX fuel with 14.3 % Pu are comparable with that of the SBR–MOX fuel in Table 16. As seen in Table 12, the difference in thermal resistivity among the three phases is significant in the irradiated condition. In this case, the effective thermal conductivity is sensitive to distribution of the three phases. Figure 25 and Figure 26 show that the MIMAS–MOX fuel with 8.4 % Pu has a more coarsely heterogeneous Pu distribution compared to that with 14.3 % Pu. This distribution in the MIMAS–MOX fuel with 8.4 % Pu results in more U agglomerate paths where the local burnup is much lower than that in the intermediate phase and Pu-rich agglomerates. These U agglomerate paths have low thermal resistivity because of their lower burnup and can, therefore, serve as fast paths for phonon conduction. This fast-path effect is reflected in the effective thermal conductivities through the evaluation using Equation (28). At 68 GWd/t-HM, therefore, the effective thermal conductivity of the MIMAS–MOX fuel with 8.4 % Pu is significantly higher than that of the SBR–MOX fuel with 8.4 % Pu. On the other hands, the three phases in the MIMAS–MOX fuel with 14.3 % Pu are distributed more homogeneously or at random compared to those in the MIMAS–MOX fuel with 8.4 % Pu, as shown in Figure 25 and Figure 26. This distribution decreases the fast-path effect and resulted in the effective thermal conductivity close to that of SBR–MOX fuel even in irradiated condition. Accordingly, the difference in the effective thermal conductivity between the two MIMAS–MOX fuels becomes larger regardless of their same burnup, compared with that in the unirradiated condition.

4-3-2 Comparison of model predictions and measurements

Figure 27 shows the effective thermal conductivities predicted by Equation (28) for the MIMAS–MOX fuels as a function of temperature, along with thermal conductivity measurements corrected to 95% theoretical density as well as predictions and measurements

for the SBR–MOX fuel. For the unirradiated fuels, no effect of heterogeneous Pu distribution on the thermal conductivity is observed between the measurements for the MIMAS–MOX and SBR–MOX fuels with 8.4 wt% Pu. As mentioned in the previous section including Table 16, the prediction using Equation (28) also indicates that there is no significant difference in thermal conductivity between the unirradiated MIMAS–MOX and SBR–MOX fuels with 8.4 % Pu. This results in overlapping of the two prediction curves in Figure 27. Consequently, the predictions for the unirradiated MIMAS–MOX and SBR–MOX fuels with 8.4 wt% Pu agree well with the measurements. Regarding the effect of Pu content, the measurements for the MIMAS–MOX fuel with 14.3 wt% Pu show lower thermal conductivity than that with 8.4 wt% Pu. The prediction shown in Figure 27 reproduces this effect of Pu content.

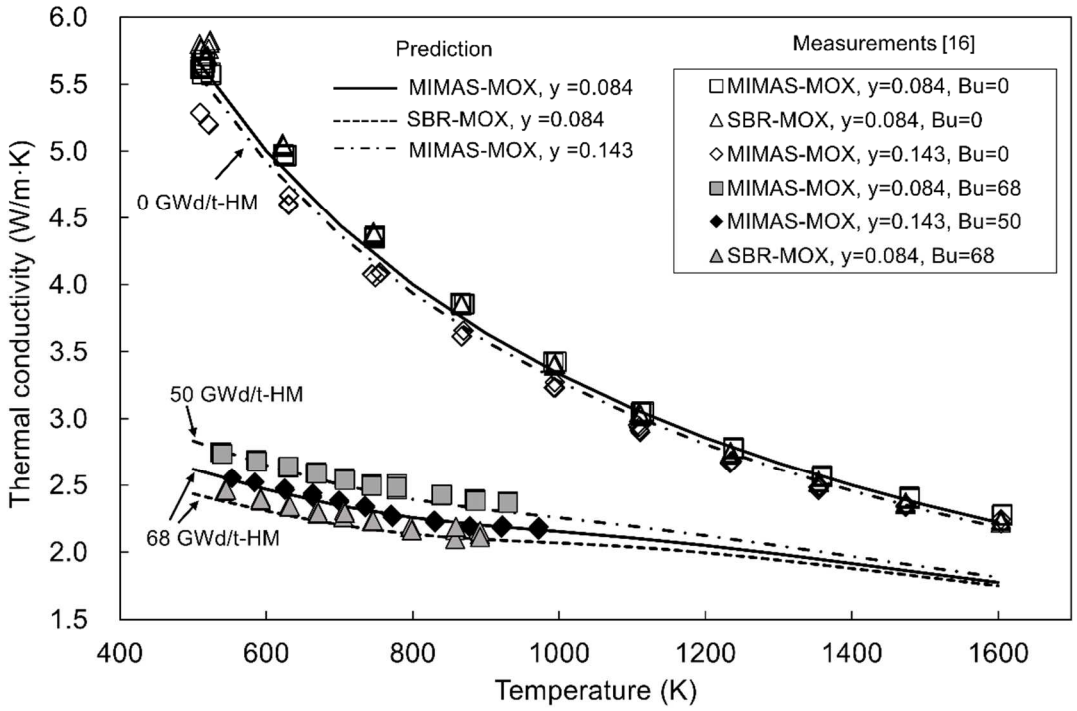


Figure 27 Comparison of prediction with measurements on thermal conductivity of MOX fuel with homogeneous and heterogeneous Pu distributions

For the irradiated fuels, the measured thermal conductivities are ranked as follows: SBR–MOX with 8.4 wt% Pu < MIMAS–MOX with 14.3 wt% Pu < MIMAS–MOX with 8.4 wt% Pu. The thermal conductivity measurements for the irradiated MIMAS–MOX fuel with 14.3 wt% Pu irradiated up to 50 GWd/t-HM are lower than that with 8.4 wt% Pu irradiated up to 68 GWd/t-HM. On the other hand, the predictions for the irradiated fuels show the ranking as follows: SBR–MOX with 8.4 wt% Pu < MIMAS–MOX with 8.4 wt% Pu < MIMAS–MOX with 14.3 wt% Pu. Since burnup has a greater effect on thermal conductivity than heterogeneous Pu distribution in Equation (28), Equation (28) basically predicts a higher thermal conductivity for the fuel with a lower burnup. Accordingly, the predicted thermal conductivity for the 14.3 wt% Pu MIMAS–MOX fuel irradiated up to 50 GWd/t-HM is higher than that for the 8.4 wt% Pu MIMAS-MOX fuel irradiated up to 68 GWd/t-HM in Figure 27. This is the opposite to the measurements. It is important to note the 10% uncertainty in the measurements [11][37]. The 10 % uncertainty can contribute to the different results between the measurements and predictions. Another possible factor is the omission of a relevant parameter in the model equations proposed in this study. Further investigation is required to resolve this inconsistency.

When comparing the MIMAS–MOX fuel with 8.4 wt% Pu irradiated up to 68 GWd/t-HM and SBR–MOX fuel with 8.4 wt% Pu irradiated up to 68 GWd/t-HM, their Pu contents and burnups are identical. Therefore, the difference in their thermal conductivities can be solely attributed to the heterogeneous Pu distribution. Indeed, the effect of the heterogeneous Pu distribution is evident in the measurements shown in Figure 18 and Figure 27. While Equation (28) adequately predicts this effect, the prediction for the MIMAS–MOX fuel with 8.4 wt% Pu slightly underestimates the measured thermal conductivity. This underestimation could be attributed to an overestimation of the thermal resistivity of the Pu-rich agglomerates in the model formula or equivalently, an underestimation of the thermal conductivity. As shown in Table 12, the burnup of the Pu-rich agglomerate with a Pu fraction of 0.177 is estimated at 127 GWd/t-HM. Figure 28 shows the effect of fission products on thermal resistivity, represented by h_1(Bu) in Table 10. It shows that the thermal resistivity caused by fission products increases

linearly with burnup. However, the linear effect of fission products has only been verified up to approximately 61 GWd/t-HM [58]. The burnup of 127 GWd/t-HM is considerably beyond this verified range. Lucuta et al. [64] showed that precipitated fission products contributed positively to thermal conductivity at high burnup. Ronch et al. [27] also showed that the formation of the high burnup structure has a positive effect on the lattice thermal conductivity, and that the degradation of thermal conductivity of UO_2 fuel with burnup saturated at a burnup of approximately 75 GWd/t-HM. Recently, Magni et al. [65] proposed a model formula to calculate the thermal conductivity of MOX fuel, verified up to a Pu content of 45 wt% and a burnup of 130 GWd/t-HM. According to their model formula, the thermal conductivity of MOX fuel with a Pu fraction of 0.177, irradiated to 127 GWd/t-HM, is calculated to be 2.37 W/m·K at 1000 K. This corresponds to a thermal resistivity of 0.422 m·K/W, which is lower than 0.618 m·K/W in Table 12. Bonev et al. [66] reported that the thermal conductivity of MOX fuel with an initial Pu content of 22 mol%, irradiated up to 12.5 %FIMA (117 GWd/t-HM) exceeded 3.0 W/m·K at 1000 K. This corresponds to a thermal resistivity of less than 0.333 m·K/W, which is also lower than the value of 0.618 m·K/W listed in Table 12. Considering these studies, we adjusted the effect of fission products, $h_1(Bu)$ in Table 10, to ensure that the effective thermal conductivity calculated from Equation (28) aligns with the measurements for the irradiated MIMAS–MOX fuel in Figure 27. We now propose Equation (30) to represent the effect of fission products on thermal resistivity, replacing the linear effect shown in Table 10.

$$\boldsymbol{h1(Bu) = 2.45 \times 10^{-3} \cdot Bu - 1 \times 10^{-5} \cdot Bu^2} \quad (30)$$

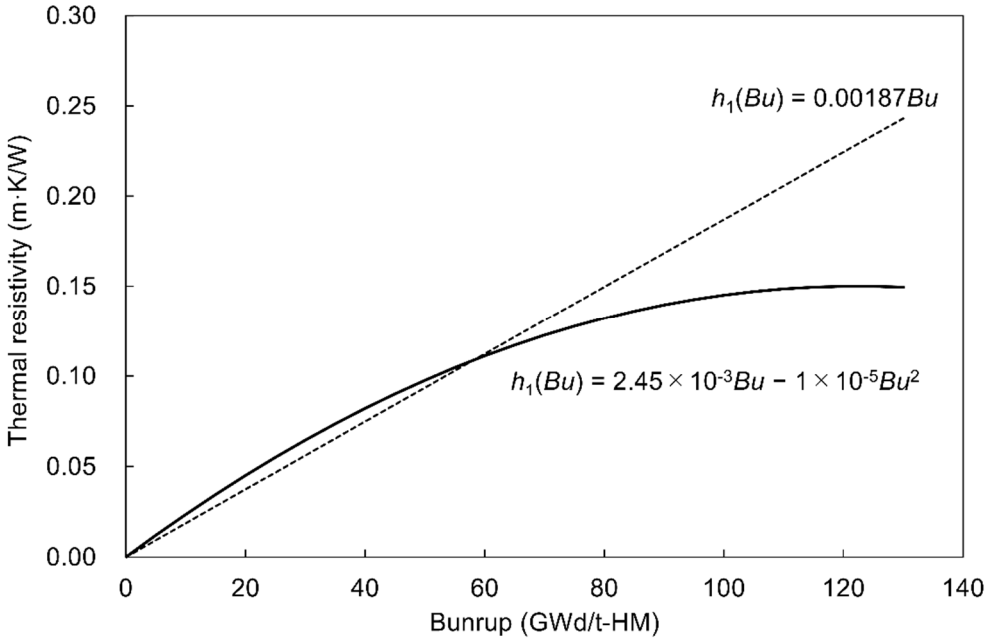


Figure 28　Effect of fission products on thermal resistivity as a function of burnup

Figure 29 shows the prediction using Equation (30) and measurements for the MIMAS–MOX with 8.4 wt% Pu and SBR–MOX fuels with 8.4 wt% Pu. The prediction and measurements agree better than those in Figure 27. Note that the predictions for the unirradiated MIMAS–MOX and SBR–MOX fuels are overlapped in Figure 29. Finally, it is confirmed that the model formula presented as Equation (28) accurately represents the thermal conductivity of both unirradiated and irradiated MIMAS–MOX fuels, taking into account heterogeneous Pu distribution.

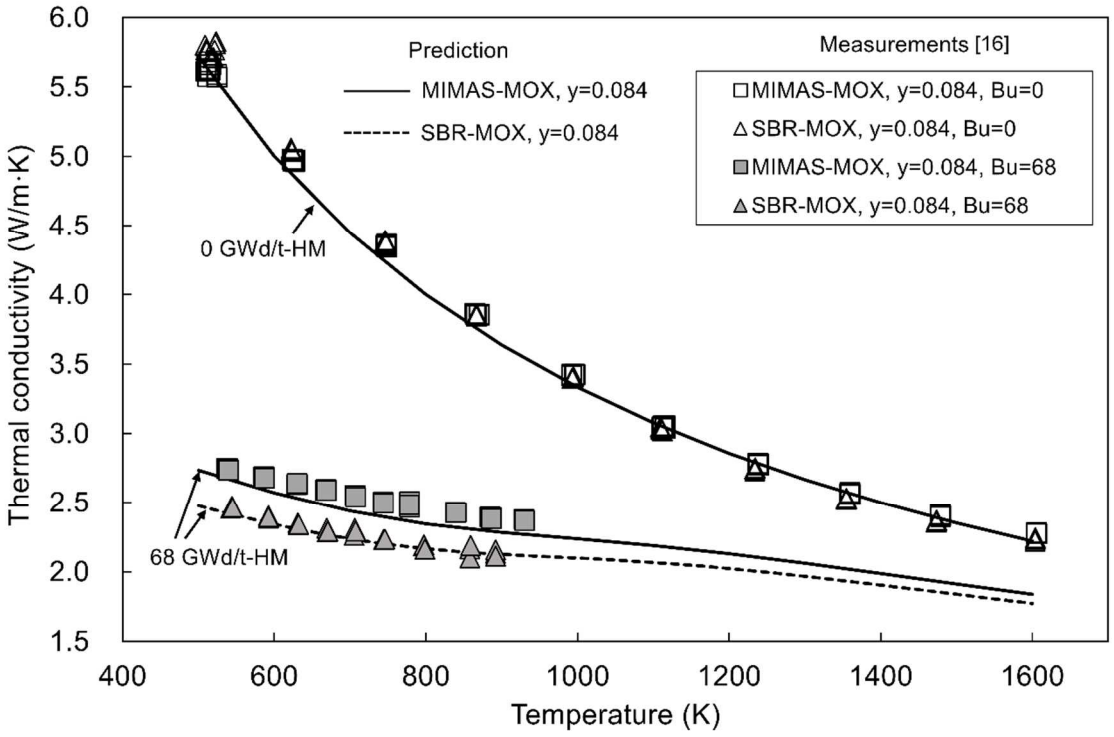


Figure 29 Comparison of prediction with measurements on thermal conductivity of MOX fuel with homogeneous and heterogeneous Pu distributions with the identical Pu content and burnup

5. Conclusion

The objectives of this study, that are to explain the mechanism how the heterogeneous Pu distribution affects the overall thermal conductivity and to formulate its effect for MIMAS-MOX fuel, have been accomplished through the following studies.

In Chapter 2 following the introduction in Chapter 1, we studied the thermal conductivity of single crystalline UO_2 and polycrystalline UO_2. The study revealed that the thermal conductivity of UO_2 is independent of crystal grain size, in other words, grain boundary gives no effect on the phonon scattering in UO_2 within the typical operating temperature range of light water reactors. In the mixed oxide, $(U, Pu)O_2$, Pu atoms replace U atoms at cation sites. This replacement does not influence the state of grain boundaries. Therefore, we considered only Pu atoms, lattice defects and fission products as phonon scattering sources which work to degrade the thermal conductivity of unirradiated and irradiated MOX fuel, excluding grain boundaries. Furthermore, a formula expressing the thermal resistivity of unirradiated UO_2 was derived from analysis of the thermal conductivity measurements.

In Chapter 3, we presented detailed analyses of both unirradiated archive MOX fuel samples and irradiated MOX fuel samples. Elemental analysis using EPMA confirmed heterogeneous Pu distribution in the MIMAS-MOX fuel samples. It was also confirmed that the distribution of a fission product neodymium in the MIMAS-MOX fuel samples was coincident with the Pu distribution. In addition to the elemental analysis, Chapter 3 provided the measurements of the thermal conductivity of MIMAS-MOX fuel with heterogeneous Pu distribution fuel and SBR-MOX fuel with homogeneous Pu distribution in both unirradiated and irradiated states. These measurements showed the effect of Pu distribution on the thermal conductivity.

In Chapter 4, we focused on thermal resistivity rather than thermal conductivity. We first proposed the constitutive formula (Equation (13)) to describe the thermal resistivity of homogeneous MOX fuel based on the phonon scattering theory. The elemental components of the constitutive formula represent the thermal resistivity of unirradiated UO_2 (Equation (3)), the

burnup effect (Equation (20)), and the impurity effect of Pu (Equation (21)), respectively. The prediction using the constitutive formula (Equation (13)) agreed well with the measurements for the SBR-MOX fuel with homogeneous Pu distribution. Next, we proposed a method to derive the effective thermal conductivity of MOX fuel with heterogeneous Pu distribution based on the concept of thermal resistance circuits. Using this method and Pu concentration maps obtained via EPMA in Chapter 3, we derived a formula to express the effective thermal conductivity (Equation (28)) and predicted values for the MIMAS–MOX fuels. Comparison between the predicted effective thermal conductivity of the MIMAS–MOX fuels and experimental measurements demonstrated the good applicability of the proposed formula (Equation (28)) for estimating the thermal conductivity of both unirradiated and irradiated MIMAS–MOX fuels, accounting for the heterogeneous Pu distribution. These findings explain that U agglomerates in MIMAS–MOX fuel, serve as fast pathways for phonon conduction. This effect is particularly pronounced in irradiated MIMAS–MOX fuel, resulting in higher thermal conductivity compared to SBR–MOX fuel, especially at high burnup. The findings obtained from this study can be utilized in verifying the validity of the thermal conductivity model of MOX fuel used in design and safety evaluations.

Acknowledgements

The author would like to thank Prof. H. Muta and Prof. Y. Ohishi of the University of Osaka for their guidance and support throughout this research. I am grateful to Mr. H. Akiyama of NRA for his cooperation on the conduct of the research project on MOX fuel. Many data obtained in the research project are used in this dissertation. I also would like to extend my thanks to Dr. M. Verwerft and Dr. R. Delville of SCK-CEN, Dr. J. Noirot of CEA Cadarache, and Dr. D. Staicu of the Joint Research Centre in Karlsruhe for their great help with conducting EPMA and thermal conductivity measurement. Support from Mitsubishi Nuclear Fuel Co., Ltd. (currently Mitsubishi Heavy Industries, Ltd.) in management of the research project on MOX fuel is gratefully acknowledged.

References

[1] K. Kitano, H. Akiyama, Research on the properties of high-burnup and high plutonium content mixed-oxide fuels, J. Nucl. Mater. 572(2022) 154075.

[2] G. Oudinet, I. Munoz-Viallard, L. Aufore, et al., Characterization of plutonium distribution in MIMAS MOX by image analysis, J. Nucl. Mater., 375 (2008) 86–94.

[3] Z. Talip, S. Peuget, M. Magnin, et al., Characterization of un-irradiated MIMAS MOX fuel by Raman spectroscopy and EPMA, J. Nucl. Mater., 499 (2018) 88–97.

[4] C. Duriez, J-P. Alessandri, T. Gervais, et al., Thermal conductivity of hypostoichiometric low Pu content (U,Pu)O_{2-x} mixed oxide, J. Nucl. Mater. 277 (2000) 143–158.

[5] H. Fujii, H. Teshima, K. Kanasugi, et al., MOX Fuel Performance Experiment Specified for Japanese PWR Utilisation in the HBWR, J. Nucl. Sci. Tech., Vol. 43, No. 9(2006), 998–1005.

[6] C. Cozzo, D. Staicu, G. Pagliosa, et al., Thermal conductivity of homogeneous and heterogeneous MOX fuels with up to 44 MWd/kgHM burnup, in: Proceedings of 2008 Water reactor fuel performance meeting, Seoul, Korea, October 19–23, 2008.

[7] D. Staicu, C. Cozzo, D. Papaioannou, et al., Thermal conductivity of fresh and irradiated MOX fuel: Influence of microstructure, in: Proceedings of Top Fuel 2009, Paris, France, September 6–10, 2009.

[8] J. Nakamura, M. Amaya, F. Nagase, et al., Thermal conductivity change in high burnup MOX fuel pellet, J. Nucl. Sci. Tech., Vol. 46, No. 9(2009), 944–952.

[9] D. Staicu and D. Baron, Discussion about the main parameters affecting the thermal conductivity of LWR UO_2 and MOX fuels, in: Proceedings of 2010 LWR fuel performance/TopFuel/WRFPM, Orlando, Florida, USA, September 26–29, 2010.

[10] M. Amaya, J. Nakamura, F. Nagase, et al., Thermal conductivity evaluation of high burnup mixed-oxide (MOX) fuel pellet, J. Nucl. Mater., 414 (2011), 303–308.

[11] D. Staicu, C. Cozzo, et al., Thermal conductivity of homogeneous and heterogeneous MOX fuels with up to 44 MWd/kgHM burnup, J. Nucl. Mater., 412 (2011) 129–137.

[12] Y. Kosaka, S. Kurematsu, T. Kitagawa, et al., Thermal conductivity degradation analyses of LWR MOX fuel by the quasi-two phase material model, J. Nucl. Sci. Tech., Vol. 49, No. 10(2012), 966–974.

[13] D. Staicu and M. Baker, Thermal conductivity of heterogeneous LWR MOX fuels, J. Nucl. Mater., 442 (2013), 46–52.

[14] N. Nakae, H. Akiyama, H. Miura, et al., Thermal property change of MOX and UO2 irradiated up to high burnup of 74 GWd/t, J. Nucl. Mater. 440 (2013), 515–523.

[15] H. Muta, N. Kato, Y. Ohishi, et al., Thermal conductivity analysis of UO2 based fuel by relaxation-time approximation method, Manuscript submitted for publication in Journal of Nuclear Materials.

[16] K. Kitano, H. Akiyama, Research on the performance of mixed oxide fuel, Secretariat of Nuclear Regulation Authority, RREP-2018-1003, Japan, 2018 (Japanese), Accessed March 1, 2022, Available from https://warp.da.ndl.go.jp/info:ndljp/pid/11297219/www.nsr.go.jp/data/000253083.pdf

[17] C. W. Bale, E. Bélisle, P. Chartrand, et al., FactSage Thermochemical Software and Databases - 2010 - 2016, Calphad, vol. 54, pp 35-53, 2016.

[18] A. Eucken, Thermal conductivity of ceramic refractory materials; Calculation from thermal conductivity of constituents, Forsh. Gebiete Ingenieurw. B3 Forschunggsheft, No. 353 (1932) 16.

[19] J. C. Maxwell, A treatise on electricity and magnetism, vol. 1, Clarendon Press, Oxford (1892) 440.

[20] IAEA, Thermal Conductivity of Uranium Dioxide, Technical Reports Series - IAEA, 59 (1966) 68.

[21] J. P. Moore and D. L. Mcelroy, Thermal Conductivity of Nearly Stoichiometric Single-Crystal and Polycrystalline UO_2, J. Am. Ceram. Soc.,54 (1971) 40.

[22] K. Aring and A. J. Sievers, Thermal Conductivity and Far‐Infrared Absorption of UO_2, J. Appl. Phys., 38 (1967) 1496-1498.

[23] O. Bethoux, P. Thomas, L. Weil, Compt. Rend. Acad. Sci., 253 (1961) 2043-2045.

[24] T. G. Godfrey, W. Fulkerson, T. G. Kollie, J. P. Moore, D. L. Mcelroy, Thermal Conductivity of Uranium Dioxide from -57° to 1100°C by a Radial Heat Flow Technique, J. Am. Ceram. Soc., 48 (1965) 297-305.

[25] M. Hirai, and S. Ishimoto, Thermal diffusivities and thermal conductivities of UO_2-Gd_2O_3 J. Nucl. Sci., 28 (1991) 995-1000.

[26] D. D. Lanning, C. E. Beyer, K.J.Geelhood, FRAPCON-3 Updates, Including Mixed-Oxide Fuel Properties, NUREG/CR-6534, Vol. 4, PNNL–11513, US-NRC, May 2005.

[27] C. Ronchi, M. Sheindlin, D. Staicu, at al., Effect of burn-up on the thermal conductivity of uranium dioxide up to 100.000 $MWdt^{-1}$, J. Nucl. Mater. 327 (2004) 58–76.

[28] Z. Wang, J. E. Alaniz, W. Jang, J. E. Garay, C. Dames, Nano lett. 11 (2011) 2206.

[29] K. Kitano, H. Akiyama, N. Nakae, A methodology to predict a fission gas release ratio of MOX fuel with heterogeneous microstructure, J. Nucl. Sci. Tech. Vol. 54, No. 11 (2017) 1190–1200.

[30] K. Kitano, H. Akiyama, Y. Ohishi, et al., EPMA and EBSD observations of unirradiated MIMAS-MOX fuels for the study of fission gas release and thermal conductivity, J. Nucl. Sci. Tech. Vol. 62, No. 4 (2024) 341–352.

[31] N. Nakae, H. Ikehata, T. Baba, K. Kamimura, et al., Irradiation behavior of MOX fuel under high burnup, in: Proceedings of TopFuel 2010, Orlando, Florida, USA, September 26–29, 2010.

[32] N. Nakae, T. Baba, K. Kamimura, et al. Trend in plutonium content of MOX fuel in thermal reactor use and irradiation behavior of MOX with high plutonium content, in: Proceedings of TopFuel 2009, Paris, France, September 6–10, 2009.

[33] Introduction to EPMA, CAMECA, Accessed 25th June 2025. Available from: https://www.cameca.com/products/epma/epma-introduce

[34] R. Delville, M. Verwerft, Quantitative Microstructural Analysis by Correlative EPMA/EBSD/BSE Electron Microscopies Applied to Nuclear Ceramic, Microscopy and

Microanalysis, 29 (2023) 78–85.

[35] Standard Test Methods for Determining Average Grain Size Using Semiautomatic and Automatic Image Analysis, E1382, ASTM International.

[36] Standard Test Method for Determining Average Grain Size, E112-10, ASTM International.

[37] C. Cozzo, D. Staicu, G. Pagliosa, et al., Thermal diffusivity of homogeneous SBR MOX fuel with a burn-up of 35MWd/kgHM, J. Nucl. Mater. 400 (2010) 213–217.

[38] D.G. Martin, The thermal expansion of solid UO2 and (U, Pu) mixed oxide – A review and recommendations, J. Nucl. Mater. 152 (1988) 94–101.

[39] N. Nakae, T. Baba, K. Kamimura, Kinetics of gaseous atoms in uranium plutonium mixed oxide, in: Proceedings of ICAPP 2011, Nice, France, May 2-5, 2011

[40] R.L. Gibby, The effect of plutonium content on the thermal conductivity of (U, Pu)O_2 solid solutions, J. Nucl. Mater. 38 (1971) 163–177.

[41] S. Nichenko, D. Staicu, Molecular Dynamics study of the effects of non-stoichiometry and oxygen Frenkel pairs on the thermal conductivity of uranium dioxide, J. Nucl. Mater. 433 (2013) 297–304.

[42] H. Bailly, D. Menessier, C. Prunier, The nuclear fuel of pressurized water reactors and fast reactors design and behaviour, Commissariat à l'énergie atomique et aux énergies alternatives, France, 1999, Chapter 4, p.125.

[43] K. Tasaka, J. Katakura, H. Ihara, et al., JNDC nuclear data library of fission products - Second version, JAERI 1320, Japan Atomic Energy Agency, Japan, 1990.

[44] F. Schmitz, R. Lindner, Diffusion of heavy elements in nuclear fuels: actinides in UO_2, J. Nucl. Mater. 17 (1965) 259–269.

[45] K. Kitano, Y. Ohishi and H. Muta, Study on the effect of heterogeneous Pu distribution on the thermal conductivity of MOX fuel, J. Nucl. Mater. 618 (2026) 156212.

[46] C. Kittel, Introduction to solid state physics 6th edition, John Wiley & Sons, Inc., New York, U.S.A, 1986.

[47] D. R. Olander, Fundamental aspects of nuclear reactor fuel elements, U.S.A, 1976,

https://doi.org/10.2172/7343826

[48] J. J. Carbajo, G. L. Yoder, S. G. Popov, et al., A review of the thermophysical properties of MOX and UO2 fuels, J. Nucl. Mater., 299 (2001), Iss. 3, 181–198.

[49] M.J. Rahman, B. Szpunar, J.A. Szpunar, Comparison of thermomechanical properties of $(U_x,Th_{1-x})O_2$, $(U_x,Pu_{1-x})O_2$ and $(Pu_x,Th_{1-x})O_2$ systems, J. Nucl. Mater. 513 (2019) 8–15.

[50] Hj. Matzke, P. G. Lucuta, R. A. Verrall, et a., Specific heat of UO_2-based SIMFUEL, J. Nucl. Mater. 247 (1997) 121–126.

[51] D.G Martin, Re-appraisal of the thermal conductivity of UO_2 and mixed (U, Pu) oxide fuel, J. Nucl. Mater. 110 (1982) 73–94.

[52] Y. Philipponneau, Thermal conductivity of (U, Pu)O_{2-x} mixed oxide fuel, J. Nucl. Mater. 188 (1992) 194–197.

[53] P. G. Klemens, Thermal resistance due to point defects at high temperature, Physical review Vol. 119, No. 2 (1960) 507–509.

[54] B. Abeles, Lattice thermal conductivity of disordered semiconductor alloys at high Temperatures, Vol. 131, No. 5 (1963) 1906–1911.

[55] T. Arima, S. Yamasaki, Y. Inagaki, et al., Evaluation of thermal conductivity of hypostoichiometric (U, Pu)O_{2-x} solid solution by molecular dynamics simulation at temperatures up to 2000K, J. Alloys and Compounds 415 (2006) 43–50.

[56] S. Nichenko and D. Staicu, Molecular Dynamics study of the mixed oxide fuel thermal conductivity, J. Nucl. Mater. 439 (2013) 93–98.

[57] T. Matsumoto, T. Arima, Y. Inagaki, et al., Molecular dynamics calculations of heat conduction in actinide oxides under thermal gradient, Progress in Nuclear Energy 85 (2015) 271–276.

[58] K. Ohira and N. Itagaki, Thermal conductivity measurements of high burnup UO_2 pellet and a benchmark calculation of fuel temperature, In: Proceedings of International Topical Meeting on LWR Fuel Performance, Portland, Oregon, March 2 - 6, 1997.

[59] A. Eucken, Allgemeine Gesetzmäßigkeiten Für Das Wärmeleitvermögen

VerschiedenerStoffarten Und Aggregatzustände,Forschung Auf Dem Gebiete Des Ingenieurwesens, vol.11, no. 1 (1940) 6–22, DOI: 10.1007/BF02584103.

[60] A. L. Loeb, Thermal Conductivity: VIII, A Theory of thermal conductivity of porous materials, J. Am. Ceram. Soc. Vol. 32, Iss. 2 (1954) 96–99, https://doi.org/10.1111/j.1551-2916.1954.tb20107.x

[61] H. Kämpf and G. Karsten, Effect of different types of void volumes on the radial temperature distribution of fuel pin, Nuclear Application and Tecchology, Vol. 9 (1970) 288–300.

[62] B. Schulz, Thermal conductivity of porous and highly porous matarials, High Temperature-High Pressure, Vol.13 (1981) 649–660

[63] H. S. Lee, D. S. Kim, D-J Kim, et al., Development of thermal conductivity model with use of a thermal resistance circuit for metallic UO2 microcell nuclear fuel pellets, Nucl. Eng. Tech. 55 (2023) 3860–3865.

[64] P.G. Lucuta, Hj. Matzke, I.J. Hastings, A pragmatic approach to modelling thermal conductivity of irradiated UO_2 fuel: review and recommendations, J. Nucl. Mater. 232 (1996) 166–180.

[65] A. Magni, T. Barani, A. Del Nevo, et al., Modelling and assessment of thermal conductivity and melting behaviour of MOX fuel for fast reactor applications, J. Nucl. Mater. 541 (2020) 152410.

[66] P. Bonev, N. Chauvin, D Staicu, et al., New recommendation for the thermal conductivity of irradiated (U,Pu)O2 fuels under fast reactor conditions. Comparison with recent experimental data, J. Nucl. Mater. 577 (2023) 154326.